



1 **In-situ Rb-Sr geochronology of white mica in young metamafic and
2 metasomatic rocks from Syros: testing the limits of LA-ICP-MS/MS mica
3 dating using different anchoring approaches**

4 Jesús Muñoz-Montecinos¹, Andrea Giuliani², Senan Oesch², Silvia Volante¹, Bradley
5 Peters², Whitney Behr¹

6

7 ¹ Institute of Geology, Department of Earth Sciences, ETH Zurich

8 ² Institute of Geochemistry and Petrology, Department of Earth Sciences, ETH Zurich

9

10 * Correspondence to: Jesús Muñoz-Montecinos (jmunoz@ethz.ch)

11

12 **Abstract**

13 The recent development of LA-ICP-MS/MS has revolutionized Rb-Sr mica dating allowing to
14 obtain isotopic data within their microstructural context. While effective for old and felsic
15 materials, this method presents challenges for young metamafic and metasomatic rocks due to
16 limited radiogenic ingrowth associated with low Rb/Sr and young ages. We quantitatively
17 address these limitations by combining laser ablation ICP-MS/MS and MC-ICP-MS data for
18 coexisting white mica and epidote, respectively, for 10 Cenozoic metamorphic rocks from
19 Syros Island (Greece). White mica analyses from metamafic and metasomatic rocks yield
20 limited Rb/Sr spread, which typically does not exceed one order of magnitude ($^{87}\text{Rb}/^{86}\text{Sr} = 14$
21 to 231 for the combined dataset), and low radiogenic $^{87}\text{Sr}/^{86}\text{Sr}$ (generally <0.8), resulting in
22 high age uncertainties of typically 10 to 50% RSE, and thus hampering robust geological
23 interpretations. Epidote $^{87}\text{Sr}/^{86}\text{Sr}$ values range between ~ 0.705 and 0.708. The former (lower-
24 end) is expected for typical, unaltered metamafic materials, whereas the latter is interpreted to
25 reflect fluid-rock interaction along shear zones, with fluids derived from or having interacted
26 with more radiogenic lithologies. These atypical values suggest that a commonly assumed
27 value of 0.703 for mafic rocks may not always be representative. Anchoring white mica Rb/Sr
28 to epidote $^{87}\text{Sr}/^{86}\text{Sr}$ data improves age accuracy and precision substantially (e.g., 29 ± 17 Ma
29 vs 47.2 ± 4.4 Ma for sample SYGR36). The new ages obtained in this study are consistent with
30 multiple events previously recorded in Syros and the Cyclades blueschists unit including: i)
31 metasomatism at near-peak to epidote blueschist-facies during early exhumation (47.2 ± 3.8
32 Ma to 41.1 ± 3.1); ii) a late stage of high-pressure exhumation and metasomatism transitioning
33 to blueschist-greenschist-facies (20.8 ± 3.1 Ma to 19.8 ± 5.2 Ma). Anchored white mica Rb/Sr
34 dates thus allow us to discriminate events of fluid-rock interactions and metasomatism
35 associated with shear zone deformation at the subduction interface.

36 **Keywords**

37 Rb-Sr dating; phengite; epidote; Syros; metamorphism; metasomatism

38

39



40 **Introduction**

41 Subduction zones host a wide range of mechanical and chemical processes that occur at various
42 spatial and temporal scales including but not limited to seismicity (e.g., Muñoz-Montecinos et
43 al., 2021; Wirth et al., 2022), element and nutrient recycling/transfer (e.g., Li et al. 2021,
44 Tumiati et al., 2022; Rubatto et al., 2023), volcanism (Breeding et al., 2004) and orogenesis
45 (e.g., Burg and Bouilhol, 2019). These processes are temporally associated with metamorphism
46 and metasomatic events of rocks conforming the deep subduction zone, and occur at time-
47 scales ranging from steady-state tectonics (e.g., foliation development and nappe stacking over
48 millions of years) to nearly instantaneous mineral growth and fluid flow (John et al., 2012).
49 Constraining the timing of high-pressure and low-temperature (HP-LT) crystal growth and
50 fabric development within metamorphic lithologies that once occupied the subduction interface
51 is therefore crucial for understanding deep tectono-thermal processes occurring at depth.
52 However, geochronological studies of these HP-LT rocks are commonly challenged by the
53 difficulty of precisely determining the age of subduction-related metamorphic events.
54

55 While the U-Pb system has been conventionally employed to date metamorphic, magmatic and
56 hydrothermal events, it relies on the presence of U-bearing accessory phases such as zircon,
57 monazite, titanite, rutile, and apatite which may be scarce, too small to be targeted, or absent
58 in high-pressure metamorphic rocks (e.g., Timmermann et al., 2004; Engi et al. 2017; Holtmann
59 et al., 2022; Bastias et al., 2023; Volante et al. 2024 and reference therein). Moreover, mid- to
60 low-temperature metamorphic and metasomatic events along the burial-to-exhumation path are
61 commonly not traceable using U-Pb geochronology due to the higher closure temperature of
62 most geochronometers (e.g., Chew and Spikings, 2015). Another common problem and
63 challenging task when using U-Pb of accessory minerals to date mafic rocks is combining their
64 textures with fabric development, thus hindering the chronological link of these U-bearing
65 phases to a particular microstructure. In such cases, exploring alternative minerals and
66 systematics becomes crucial to obtaining a more comprehensive and accurate record of the
67 deformation and metamorphic history.
68

69 White mica is a common mineral in metamorphic, HP-LT lithologies that is stable throughout
70 prograde and retrograde reactions (Schmidt et al., 2004; Halama et al., 2020). Enrichment in
71 Rb makes white mica a suitable Rb-Sr geochronometer for dating subduction-related
72 metamorphic processes, also considering the high closure temperature of the Rb-Sr system at
73 static, fluid-absent conditions (500–600 °C – von Blanckenburg et al., 1989; Villa, 1998; Glodny
74 et al. 1998, 2008). While multimineral Rb-Sr internal isochron analyses of subduction zone
75 rocks have been extensively utilized, often yielding robust ages (Glodny et al., 2004, 2008;
76 Wawrzenitz et al., 2006; Bröcker et al., 2013; Kirchner et al., 2016; Angiboust and Glodny,
77 2020), significant challenges remain to be addressed. These include: i) Sr isotope
78 disequilibrium between micas and the other mineral phases, which are commonly included in
79 Rb-Sr isochronous arrays; ii) post-deformation, low-temperature magmatic alteration or fluid-
80 assisted recrystallization, which might affect pristine Rb-Sr isotope compositions; iii)
81 thermally-induced diffusion processes that can also impact the Rb-Sr record (Glodny and Ring



82 2022); and iv) potential inheritance within mica grains or across mica populations (Villa, 2016;
83 Barnes et al., 2024). Therefore, grain size, deformation, alteration and fluid availability might
84 control Rb-Sr isotope variability. For example, Glodny et al. (2008) showed that large crystals
85 of biotite partially preserved the Grenvillian Sr-isotopic composition related to granulite-facies
86 metamorphism, whereas submillimeter-sized biotite in fully re-equilibrated eclogite rocks
87 yielded a different Sr-isotopic signature due to an overprinting Caledonian eclogite-facies
88 event. These variations in mica Rb-Sr systematics, and the processes underpinning them, can
89 be addressed directly using laser ablation methods.

90

91 Although substantially less precise, in-situ Rb-Sr dating of white mica using a triple quadrupole
92 inductively coupled plasma mass spectrometer associated with a laser ablation system (LA-
93 ICP-MS/MS) offers significant advantages over conventional ID-TIMS methods. This in-situ
94 method eliminates the need for mineral separation and time-consuming chromatographic
95 column chemistry, enabling quick, cost-effective analyses. It further allows one to constrain
96 potential zoning in Rb-Sr isotope distribution (Kutzschbach and Glodny, 2024; Rösel and Zack,
97 2021) and to link multiple grain populations to specific microstructural domains, hence
98 preserving essential textural information which are otherwise inaccessible. Thus, potential age
99 variations among different white mica populations (e.g., syn- to post-kinematic grains) within
100 distinct microstructural domains such as microfolds, shear bands, and boudin necks permits a
101 more accurate interpretation of ages as shown in previous mica Rb/Sr studies of metamorphic
102 rocks by LA-ICP-MS/MS (Gou et al., 2022; Gyomlai et al., 2022, 2023a; Kirkland et al., 2023;
103 Ribeiro et al., 2023; Ceccato et al., 2024; Barnes et al., 2024).

104

105 In-situ Rb-Sr geochronology has been increasingly utilized to constrain the timing of
106 deformation events along Precambrian shear zones in felsic igneous rocks (e.g., Olieroor et al.,
107 2020; Wang et al., 2022; Ribeiro et al., 2023). For instance, Tillberg et al. (2021) targeted
108 white mica and other potassic mineral phases (e.g., illite) to constrain distinct populations of
109 Precambrian and Paleozoic brittle veins and ductile shear zones. Although age (sub-)clusters
110 were challenging to distinguish, this method showed great potential for dating multiple events
111 of fault activation and reactivation (Kirkland et al., 2023). Mica Rb/Sr studies on mafic
112 lithologies are comparatively limited. A recent study from Gyomlai et al. (2023a) on mafic
113 blueschist from the Kampos belt on Syros island (Greece) presented data on the timing of fluid-
114 rock interactions along the subduction interface. However, their large uncertainties precluded
115 the distinction between peak-pressure metamorphism, retrogression and/or partial
116 recrystallisation of white mica under blueschist- to greenschist-facies conditions. More
117 accurate age constraints were obtained by Barnes et al. (2024) for a small set ($n = 4$) of samples
118 from the Syros Island, where mica Rb/Sr dating was combined with initial Sr isotope
119 constraints provided by epidote and apatite.

120

121 These studies and the increasingly widespread application of mica Rb-Sr dating by LA-ICP-
122 MS/MS to date magmatic and hydrothermal events (e.g., Redaa et al., 2022; Wang et al., 2022;
123 Zametzer et al., 2022; Huang et al., 2023; Giuliani et al., 2024) highlights the versatility of in-
124 situ mica Rb-Sr geochronology to investigate different rock-types and geological questions.
125 However, lithologies with low Rb contents (e.g., < 30 ppm in mafic rocks) and associated low



126 Rb/Sr micas result in low accuracies of mica Rb/Sr ages, even where hundreds of analytical
127 spots were measured (Tillberg et al., 2020). This limitation is exacerbated by dating micas in
128 young (i.e., Cenozoic) metamafic rocks where ingrowth of radiogenic Sr is limited.

129

130 In this contribution we ~~aim to~~ address the current limitations of in-situ Rb-Sr dating of white
131 mica in young metamafic and metasomatic rocks that typically contain mica crystals with low
132 Rb/Sr, and provide strategies to obtain robust Rb-Sr ages from these lithologies using laser
133 ablation methods. ~~We present new data from 10 samples from Syros Island (Kampos Belt and~~
134 ~~Megas Gialos area; Greece).~~ We present new petrographic, textural and microstructural
135 analysis of greenschist- to eclogite/blueschist-facies rocks combined with laser ablation Rb/Sr
136 analyses of white mica and laser ablation multi-collector (MC) ICP-MS Sr isotope analyses of
137 epidote for 10 samples from the Syros Island (Kampos Belt and Megas Gialos Beach; Greece),
138 complemented with bulk rock Sr isotopes for some of the samples. Although the general
139 architecture and structural relationships of blueschist- to eclogite-facies rocks in Syros are still
140 debated (e.g., Keiter et al., 2011; Laurent et al., 2018; Kotowski et al., 2022), the subdivision
141 of geological units, P-T conditions and the timing of metamorphic burial and exhumation are
142 well-constrained, making Syros an ideal case study for our purpose. We demonstrate that in
143 these young (Cenozoic) metasomatic and metamafic rocks, low Rb/Sr ratios commonly
144 preclude precise dating of mica by LA-ICP-MS/MS. Anchoring the mica-based Rb-Sr isochron
145 to an initial (or ‘common’) $^{87}\text{Sr}/^{86}\text{Sr}$ provided by either a low-Rb/Sr cogenetic phase such as
146 epidote or a geologically meaningful ‘model’ (e.g., Rosel and Zack, 2021) helps circumvent
147 this problem.

148

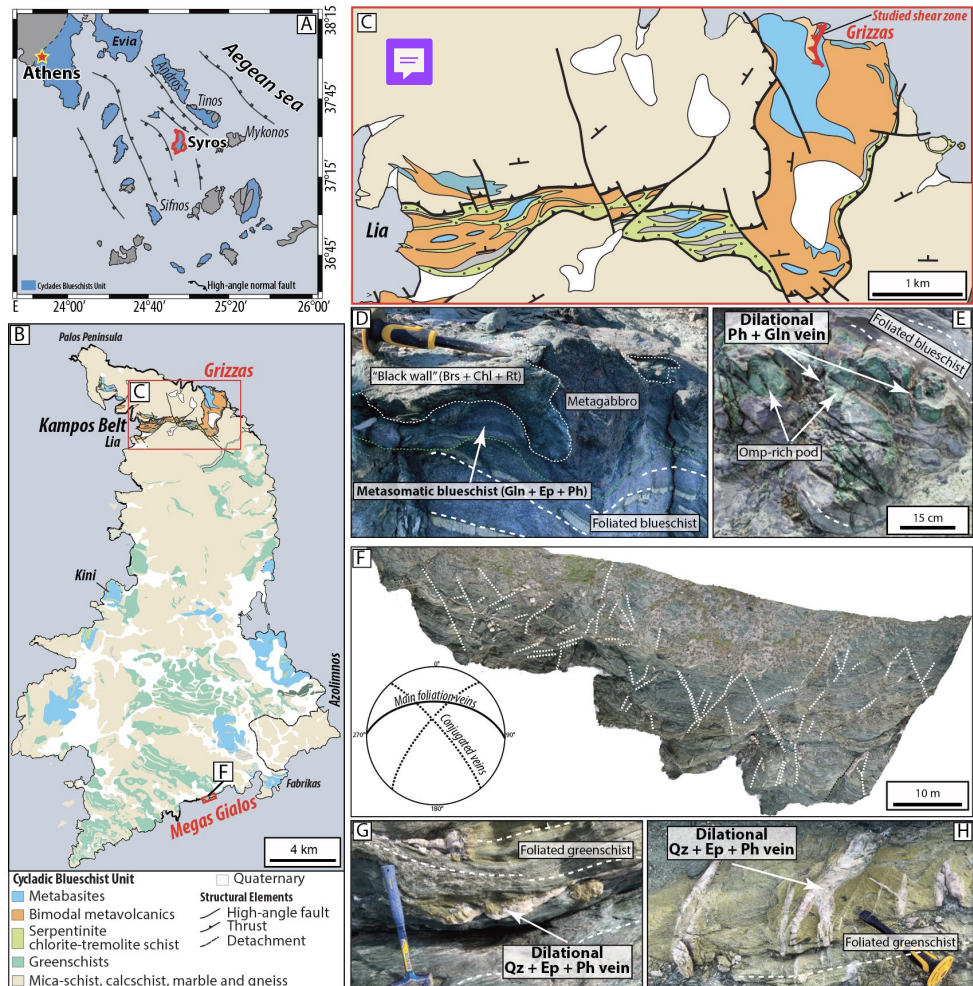
149

150

151

152

153



154
 155
 156
 157
 158
 159
 160
 161
 162
 163
 164
 165

Figure 1. A. Simplified geologic map of the Cyclades highlighting the location of Syros Island. B. Simplified geologic map of Syros Island (modified from Keiter et al., 2011); the study localities are highlighted in red. C. Zoom in of the Kampos Belt; the study locality is shown in red. D. Field image of an omphacite pod embedded in a foliated blueschist matrix within the Grizzas shear zone, the former contains some of the studied glaucophane + phengite dilational veins (sample SYGR41). E. Representative field image of metasomatic rocks from the Grizzas shear zone; note the occurrence of smeared metagabbro blocks surrounded by metasomatic rinds and black walls within a foliated blueschist and a chlorite-tremolite schists matrix. F. Orthomosaic image from the Megas Gialos outcrop (inset from panel B; modified from Muñoz-Montecinos and Behr, 2023). The lower-hemisphere stereoplot depicts the orientation of the veins following the main foliation as well as those sets oblique to it (dashed white lines illustrate the orientation of conjugated vein sets), represented here by samples SYMG08.3 and SYMG02, respectively. G and H. Examples of dilational veins containing epidote fibers along with phengite.



166 Geological setting

167 Syros Island

168 The HP-LT (~~high pressure, low temperature~~) rocks from Syros Island belong to the Cyclades
169 Blueschists Unit (CBU) cropping out along the Aegean Sea (**Figure 1A and 1B**). The CBU is
170 interpreted to represent exhumed fragments of the subducted Adriatic plate and HP-LT meta-
171 ophiolites of a northward-dipping subduction event between the Eurasian and African plates
172 (Gautier and Brun, 1994; Jolivet et al., 2010; Soukis and Stockli, 2012). The CBU is subdivided
173 into three subgroups (Glodny and Ring, 2022), from which the Top and Middle CBU nappes
174 are relevant for this study. The Top CBU nappe crops out in Syros as a narrow belt, known in
175 the literature as the Kampos Belt, to which one of the study localities belong to: the Grizzas
176 shear zone (**Figure 1C**). It is composed of abundant metavolcanic materials with a bimodal
177 composition (mafic and felsic) along with metagabbros, serpentinites, tremolite-chlorite, talc-
178 and garnet schists (Keiter et al., 2011). The Kampos Belt lithologies reached peak blueschist-
179 to eclogite-facies conditions of 480–560°C and 1.6–2.2 GPa (e.g., Trotet et al., 2001; Laurent
180 et al., 2018; Cisneros et al., 2020). The Middle CBU nappe is the most abundant unit and is
181 mainly composed of a relatively coherent intercalation of marbles, metasediments and
182 metabasites (**Figure 1B**). This latter lithotype represents the studied lithology at the Megas
183 Gialos locality (**Figure 1B and 1F**), displaying a pervasive exhumation overprint transitioning
184 from blueschist- to greenschist-facies from 450 to 400 °C and 1.4 to 1.0 GPa (Cisneros et al.,
185 2020). These retrograde metamorphic conditions are associated with transient brittle fracturing
186 and dilatational veining (Muñoz-Montecinos and Behr, 2023), from which the investigated
187 samples from Megas Gialos were collected.

188 The pre-subduction architecture of the CBU resulted from Triassic rifting of the basement
189 accompanied by deposition of passive margin sediments and carbonates (Keay, 1998; Seman
190 et al., 2017). Rifting occurred at c. 80 Ma, thinning the lithosphere and producing small-scale
191 oceanic basins along with passive margin depocenters (Keiter et al., 2011; Cooperdock et al.,
192 2018; Kotowski et al., 2022). In the Kampos Belt (Gryzzas locality), U-Th-Pb SHRIMP zircon
193 analyses in a metagabbro and a meta-plagiogranitic dike reveal two age populations, one at c.
194 80 Ma and a second one at 52.4 ± 0.8 Ma (Tomaschek et al., 2003). The older age likely reflects
195 the magmatic crystallization, whereas the younger one dates the HP-LT peak metamorphism.
196 Phengite and multi-mineral Rb-Sr (e.g., white mica + epidote + glaucophane +/- omphacite +/-
197 garnet), phengite Ar-Ar and garnet Lu-Hf ages (mostly from the Lia side, hereafter referred to
198 as the Western Kampos Belt) are in the range of 55 to 44 Ma, and were interpreted to reflect
199 the timing of prograde-to-peak HP-LT metamorphism (see Kotowski et al., 2022 and
200 references therein). The initial stage of exhumation under blueschist-facies conditions likely
201 began at c. 44 Ma, and transitioned to greenschist-facies conditions between 34 and 20 Ma
202 based on Ar-Ar and Rb-Sr multi-mineral (e.g., white mica + epidote + albite) geochronology
203 (e.g. Putzlitz et al., 2005; Uunk et al., 2018; Glodny and Ring, 2022 and references therein).
204 Gyomlai et al. (2023a) obtained in-situ mica Rb-Sr ages from a single, c. 2 m-thick outcrop in



205 the range of 52.5 ± 11.6 to 12 ± 3.1 Ma, inferred to date metasomatism of metamafic rocks
206 during HP and fluid-rock interaction during late exhumation, respectively. Multi-mineral and
207 in-situ white mica Rb-Sr and Ar-Ar dating in the Middle CBU nappe yielded peak HP-LT
208 metamorphism ages of 45 to 37 Ma, whereas the pervasive blueschist- to greenschist-facies
209 metamorphism is dated at c. 39 to 19 Ma (Glodny and Ring 2022; Barnes et al., 2024; Kotowski
210 et al., 2022 and references therein).

211 Samples and Petrography

212 In this section, we present key petrographic observations of the 10 samples from the Syros
213 Island that have been selected for Rb-Sr dating (**Table 1**), emphasizing the textural context of
214 white mica and epidote. Two additional samples (SYGR50 and SYGR44) have been analyzed
215 for epidote $^{87}\text{Sr}/^{86}\text{Sr}$ only. The investigated samples were carefully selected in order to
216 constrain the timing of fluid-rock interactions (metasomatism and veining) and to evaluate the
217 significance of $^{87}\text{Sr}/^{86}\text{Sr}$ isotopic values for anchoring white mica Rb-Sr isochrons. We targeted
218 our samples based on the presence of white mica in apparent textural equilibrium with epidote
219 (where present) and, for the Grizzas samples, the apparent absence of greenschist-facies
220 overprinting.

221 The samples coded SYGR ($N_{\text{dated}} = 7$; $N_{\text{total}} = 9$) all belong to the Grizzas locality in the
222 easternmost part of the Kampos Belt (**Figure 1B and 1C**). These samples were collected along
223 a north-dipping shear zone (hereafter referred to as the Grizzas shear zone), which juxtaposes
224 a massive to variably strained white metagabbro and blueschist-facies igneous breccia,
225 representing a region of high and localized strain (**Figure 1C**; see also Keiter et al., 2011).
226 Samples SYGR36 and SYGR44 correspond to relict (partially digested) blueschist blocks,
227 while sample SYGR50 represents a pristine, low-strain metagabbro. SYGR37 and SYGR38
228 represent the metasomatized mafic matrix wrapping around the metagabbro and blueschist
229 blocks (i.e., metasomatic rinds in **Figure 1D**), whereas sample SYGR42 is an altered
230 metagabbro (see **Table 1** for a summary of the studied samples). For comparison, a
231 metasedimentary rock sample (SYGR45) from a c. 70 cm thick discrete layer within the shear
232 zone as well as a felsic pod (sample SYGR58) contained within a moderately-strained meta-
233 igneous breccia (e.g., Keiter et al., 2011), were also targeted for dating. We emphasize the
234 occurrence of dilatational phengite + glaucophane veins (such as sample SYGR41) cross-cutting
235 omphacite pods (**Figure 1E**). The samples coded SYMG were collected from a retrograde
236 greenschist-to-blueschist-facies sliver located in the Megas Gialos locality (**Figure 1F**). The
237 selected vein samples SYMG02 and SYMG08.3 (**Figure 1G and 1H**) formed as dilatational
238 fractures related to the ascent of deep subduction zone fluids towards the base of the fore arc
239 during the latest stages of HP-LT exhumation and extension (e.g., Muñoz-Montecinos and
240 Behr, 2023). Sample SYMG07 represents the greenschist host rock associated with the vein
241 samples SYMG02 and SYMG08.3



Table 1. Sample summary

Sample ID	Rock type and general structure	Mineral assemblage	Analysed microdomain
<i>Grizzas shear zone (NE Syros)</i>			
<i>Blueschist-facies</i>			
SYGR36	Strongly foliated blueschist block	Gln + Ep + Wm + Gte + Omp + Rt	Wm defining the main foliation and pressure shadows around Gte
SYGR37	Moderate to strongly foliated metasomatic rind	Gln + Ep + Wm + Chl	Wm defining the main foliation
SYGR38	Weakly foliated metasomatic rind	Gln + Ep + Wm + Chl	Randomly oriented and interlocked Wm and Ep
SYGR41	Dilatational vein	Gln + Wm	Randomly oriented laths of Wm
SYGR42	Moderately foliated metagabbro	Gln + Wnc + Omp + Ep + Wm + Rt	Shear bands defining the main foliation
SYGR44	Moderately foliated blueschist block	Gln + Lws (now Ep + Wm) + Wm + Gte + Rt	Ep replacing Lws pseudomorphs
SYGR45	Foliated metasediment	Wm + Gln + Gte + Ep + Tur	Wm aligned and oblique according to the main foliation
SYGR50	Weakly to moderately foliated metagabbro	Omp + Ep + Gln + Wm	Ep defining the main foliation and within boudin necks
SYGR58	Moderately foliated felsic pod	Qz + Wm	Wm aligned and oblique according to the main foliation
<i>Megas Gialos (SE Syros)</i>			
<i>(HP)Greenschist-facies</i>			
SYMG02	Dilatational vein	Qz + Ep + Wm + Ab	Ep fibers and Wm laths in close contact
SYMG07	Moderately to strongly foliated	Ep + Ab + Chl + Act + Wm + Ttn	Ep and Wm defining the main foliation
SYMG08.3	Dilatational vein	Qz + Ep + Wm	Ep fibers and Wm laths in close contact

243

244 **Blueschists, blueschist-facies metagabbro and greenschist**

245 Samples SYGR36 and SYGR44 are relict blueschist blocks within a metasomatized sheared
 246 matrix. Glauconphane, together with white mica and epidote define the penetrative foliation.
 247 Texturally, white mica occurs as medium-grained laths and displays no evidence of kinks,
 248 undulose extinction or ~~mica~~ fish. In sample SYGR36, white mica also occurs within pressure
 249 shadows (**Figure 2A**) and boudin necks around garnet as well as oblique to the main foliation.
 250 No significant chemical zoning patterns were observed (**Supplementary Figure S1A**). Mostly,
 251 white mica ~~crystals~~ defining the main foliation as well as those spatially related to pressure
 252 shadows were targeted for dating. Sample SYGR44 texturally preserves lozenge-shaped
 253 lawsonite pseudomorphs now composed of strain-free epidote (targeted for $^{87}\text{Sr}/^{86}\text{Sr}$ analyses)
 254 and white mica (**Supplementary Figure S1G**).
 255

256 Sample SYGR50 is a low-strain ~~white~~ metagabbro composed of coarse-grained clinopyroxene
 257 pseudomorphs (now glauconphane, winchite and omphacite) in a matrix of epidote. The (weak)
 258 foliation is defined by elongated tabular crystals of epidote and subordinate white mica. Boudin
 259 necks within large porphyroclasts are filled by epidote, white mica and garnet (**Supplementary**
 260 **Figure S1H**). In this sample, epidote crystals defining the foliation and filling the boudin necks



261 were targeted for $^{87}\text{Sr}/^{86}\text{Sr}$ analyses. Overall, this sample represents the weakly-metasomatized
262 analogue of the altered metagabbro sample SYGR42.

263

264 Sample SYMG07 is a coarse-grained greenschist and represents the host rock associated with
265 the vein samples SYMG02 and SYMG08.3. The main foliation is defined by amphibole and
266 epidote, oriented laths of chlorite and white mica as well as stretched albite (**Figure 2B**).
267 Phengite grains from the matrix display weak core-mantle zoning patterns noticeable in back-
268 scattered electron imaging (**Supplementary Figure S1B**). The core of large white mica
269 crystals were targeted for dating, while the foliated matrix epidote was targeted for $^{87}\text{Sr}/^{86}\text{Sr}$
270 determinations, since these are interpreted as part of an equilibrium assemblage.

271 **Metasomatic rinds, metasomatized metagabbro and veins**

272 Samples SYGR37 and SYGR38 represent the matrix wrapping around metagabbro and
273 blueschist blocks. These samples are coarse-grained, foliated schists composed mainly of
274 glaucophane, epidote, phengite and chlorite. White mica from both metasomatic rinds are
275 medium to coarse-grained and occur in sharp contact with glaucophane and epidote, displaying
276 no significant chemical zoning patterns were observed nor textural evidence of recrystallization
277 (**Figures 2C and 2D**). Sharp contacts between white mica and epidote suggest textural
278 equilibrium between them (**Supplementary Figure S1C**). Thus, we targeted these
279 microdomains for white mica dating and $^{87}\text{Sr}/^{86}\text{Sr}$ determinations.

280

281 Sample SYGR42 is an altered metagabbro composed of porphyroclasts of Na-Ca amphibole
282 and omphacite after igneous clinopyroxene in a matrix of epidote and glaucophane (**Figure**
283 **2E**). Two generations of epidote, spatially associated with two distinct microdomains, are
284 observed. The first epidote generation grew as fine-grained, now heavily smeared crystals
285 occupying the interstitial matrix between porphyroclasts. This texture likely reflects epidote
286 growth after igneous plagioclase and subsequent deformation. The second epidote generation
287 grew in microdomains where a discontinuous foliation composed of tabular glaucophane and
288 epidote in sharp contact with white mica, wrapped around porphyroclasts and the fine-grained
289 epidote matrix. Within this second microdomain, white mica is medium- to coarse-grained and
290 displays evidence of recrystallization and subgrains. For this reason, coarse-grained white mica
291 crystals displaying no textural evidence for recrystallization, such as subgrains, kinks and
292 undulose extinction, were carefully selected for dating, whereas euhedral and tabular epidote
293 crystals in sharp contact with white mica crystals were targeted for $^{87}\text{Sr}/^{86}\text{Sr}$ analysis.

294

295 Sample SYGR41 is a glaucophane + white mica dilatational vein cross-cutting an omphacite
296 pod. These veins display up to centimeter-sized and randomly oriented laths of white mica
297 (**Figure 2F**) displaying no evidence of deformation nor chemical zoning (**Supplementary**
298 **Figure S1D**).

299

300 Samples SYMG02 and SYMG08.3 are dilatational veins crosscutting the foliated greenschist
301 hosts. Elongated epidote crystals occur spatially associated with white mica in sharp contact
302 suggesting contemporaneous precipitation from a fluid phase (**Figures 2G and 2H**). White

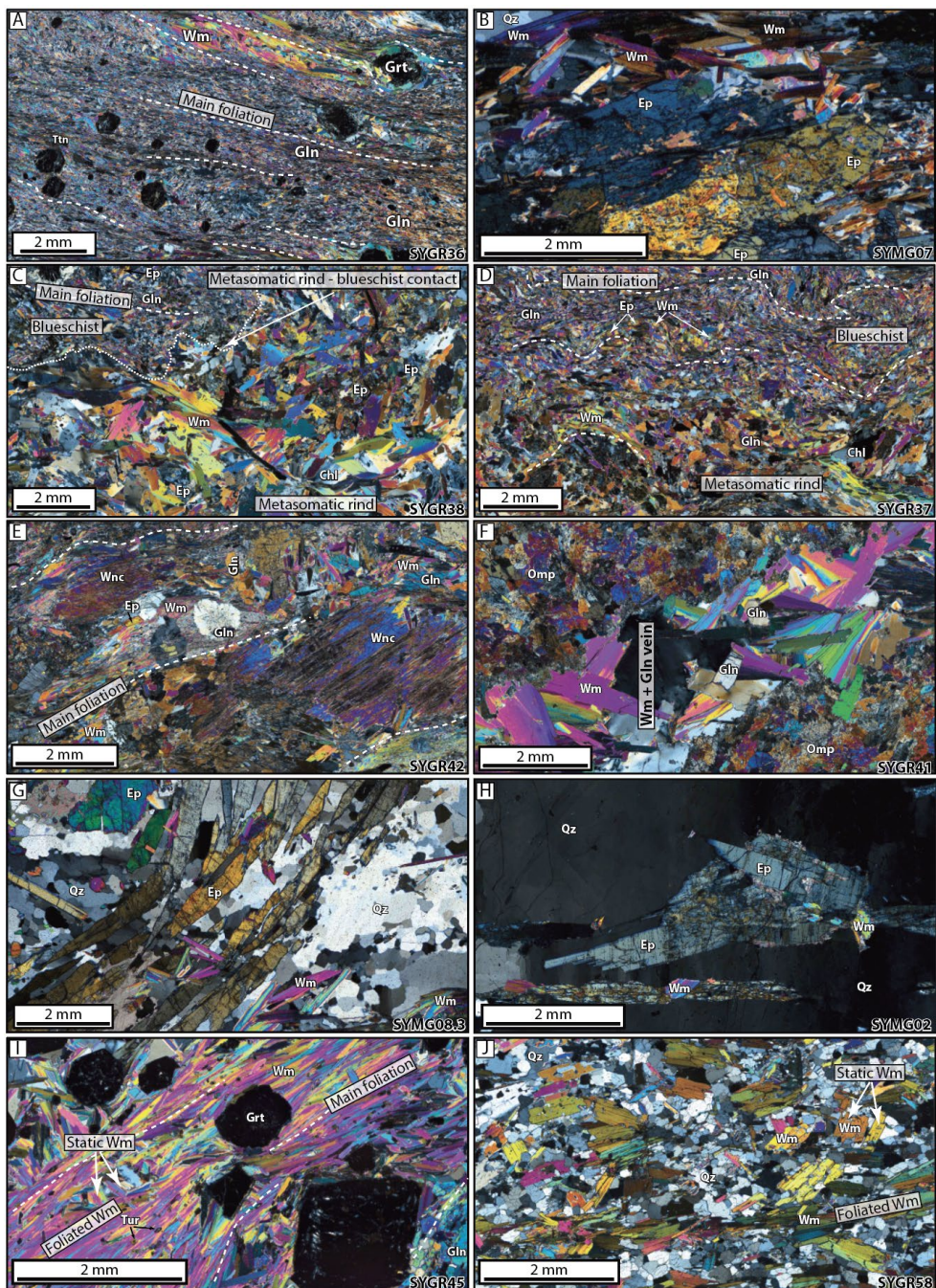


303 mica occur as euhedral, hundreds of μm long laths and correspond to strain free crystals with
304 no to faint chemical zoning (**Supplementary Figures S1E and S1F**). Thus, the most coarse
305 and pristine (e.g., unfractured) crystals were selected for white mica dating and epidote
306 $^{87}\text{Sr}/^{86}\text{Sr}$ analyses.

307 **Metasedimentary rock and felsic pod**

308 Sample SYGR45 is a well foliated garnet, glaucophane, tourmaline, mica schist with minor
309 epidote (**Figure 2I**). Texturally, the foliated white mica generation is apparently overgrown by
310 a second, static generation characterized by laths oriented oblique to the main foliation (**Figure**
311 **2E**). To avoid potentially retrograde rims, cores of large crystals defining the pervasive
312 foliation and those of crystals oblique to it were targeted for dating. However, the resulting
313 ages for these two white mica generations were indistinguishable within uncertainty, therefore
314 the final age for this sample was calculated by clustering both datasets (see below).
315

316 Sample SYGR58 is a felsic pod contained within the blueschist-facies meta-igneous breccia.
317 They are composed mostly of quartz and phengite and subordinate epidote and garnet, the latter
318 typically replaced by chlorite. A first white mica generation defines the foliation, whereas a
319 second generation of laths are oriented oblique to it (**Figure 2J**). Although the two white mica
320 generations were separately targeted for dating, the resulting ages overlap and were merged for
321 the final sample age calculation (see below).
322
323
324
325
326
327
328
329
330



331

332 **Figure 2.** Photomicrographs (crossed polars) of the dated samples. A. General overview of the blueschist block
333 sample SYGR36 emphasizing the distribution of white mica along the foliation and typically around garnets
334 forming pressure shadows. B. General fabric of the greenschist sample SYMG07 displaying the association
335 between foliated epidote and white mica. Due to the significant amount of inclusions within epidote, only the
336 inclusion-free regions were targeted for laser ablation MC-ICP-MS analysis. C. Contact between altered
337 blueschist and metasomatic rind in sample SYGR38; note the relatively curvy-sharp contact between these two



338 domains as well as the relatively larger abundance of coarse grained white mica in the latter. D. Contact between
339 altered blueschist and metasomatic rind in sample SYGR37. In this case, the contact is moderately- to highly-
340 strained resulting in a more diffuse appearance. E. Metasomatized metagabbro sample SYGR42 displaying
341 clinopyroxene pseudomorph porphyroclasts (now replaced by amphibole) in a foliated matrix composed of white
342 mica, glaucophane and epidote. F. Dilational vein cross-cutting an omphacite pod (sample SYGR41) with
343 strain-free, millimeter-sized white mica crystals in association with glaucophane. G. Dilational white mica +
344 epidote + quartz vein (sample SYMG08.3) with a texture characterized by epidote fibers and white mica laths. H.
345 Dilational white mica + epidote + quartz vein (sample SYMG02) displaying coarse-grained epidote in sharp
346 contact with finer-grained white mica. I. Metasedimentary rock sample SYGR45 highlighting white mica crystals
347 oriented parallel and oblique (static) to the main foliation as well as developing pressure shadows around garnet.
348 J. Felsic pod sample SYGR58 highlighting the distribution of white mica along the main foliation as well as some
349 grains oriented oblique to it in a matrix of quartz. Mineral abbreviations are from Whitney and Evans (2010).
350 Chl – chlorite; Ep – epidote; Gln – glaucophane; Grt – garnet; Omp – omphacite; Qz – quartz; Ttn – titanite;
351 Tur – tourmaline; Wm – white mica; Wnc – winchite.

352 Methods

353 Laser ablation MC-ICP-MS

354 In-situ Sr isotope analyses of epidote were undertaken in two separate sessions (March 2023
355 and February 2024) using an ASI RESolution 193 nm excimer laser ablation system interfaced
356 to a Nu Plasma II MC-ICP-MS at ETH Zürich ~~and~~ following a similar approach to that of
357 Fitzpayne et al. (2023) and Pimenta Silva et al. (2023). Analytical conditions included 80-100
358 μm spot size, a repetition rate of 5 (Mar-23) and 10 Hz (Feb-24), and laser fluence of \sim 4.0
359 (Mar-23) and 2.5 J/cm^2 (Feb-24). Each analysis consisted of a sequence of 40 seconds of
360 ablation and 45 seconds of washout and gas blank measurement. Total Sr signals varied widely
361 from \sim 1 to 15 V depending on the sample (**Supplementary Table S1**). Data reduction,
362 including corrections for isobaric interferences (Kr, Ca dimers, Ca argides, Rb) and
363 instrumental mass bias was performed using Iolite 4 (Paton et al., 2007, Paton et al., 2011).
364 Instrumental drift was evaluated by repeated measurement of clinopyroxene BB-1 (Neumann
365 et al., 2004; Fitzpayne et al., 2020), which was ablated every block of 15 unknowns including
366 secondary clinopyroxene standards (JJG1414; YY09-04; YY09-47; YY12-01) from Zhao et
367 al. (2020) (results included in **Supplementary Table S1**). All the data are reported relative to
368 BB-1 of $^{87}\text{Sr}/^{86}\text{Sr}$ of 0.704468 (Fitzpayne et al., 2020) via standard bracketing. $^{84}\text{Sr}/^{86}\text{Sr}$ of
369 clinopyroxene standards and epidote unknowns are generally within uncertainty of the natural
370 ratio (\sim 0.0565). $^{87}\text{Rb}/^{86}\text{Sr}$ ratios are negligible (typically <0.001), which makes corrections for
371 ^{87}Sr ingrowth insignificant. Therefore, the reported Sr isotope ratios are considered to be equal
372 to the initial Sr isotope ratios at time of epidote crystallization.

373 Laser ablation ICP-MS/MS

374 In-situ Rb-Sr isotope analyses of white mica in thin section were undertaken during two
375 sessions (October 2022 and May 2023) using an ASI RESolution 193 nm excimer laser probe
376 interfaced to an Agilent 8800 ICP-MS/MS at ETH Zürich ~~following the procedure outlined in~~
377 Giuliani et al. (2024) and Ceccato et al. (2024). ~~The mass spectrometer was first~~
378 ~~tuned in single-quad mode (i.e. no gas in the collision cell) to~~



379 optimize the Rb and Sr signals by ablating NIST612. Oxide production
380 rate based on measurement of ThO/Th in NIST612 was ≤ 0.2 wt.%. After
381 introducing ultrapure N₂O gas (>99.99%) in the reaction cell (flow rate of 0.23-0.25
382 mL/min), a second tuning step was undertaken by ablating NIST610 to maximize production
383 of SrO⁺ ions while maintaining high sensitivity for Rb⁺ ions. Interaction of Sr⁺ ions with N₂O
384 resulted in conversion of ~89% of Sr⁺ ions to SrO⁺ based on monitoring of masses 88 (Sr⁺),
385 104 (SrO⁺) and 105 (SrOH⁺). No detectable RbO⁺ was recorded. Analytical conditions for mica
386 analyses included 80-100 μ m spot size, a pulse rate of 5 Hz, and laser fluence of ~ 3.5 -4.0 J/cm².
387 Each analysis consisted of a sequence of 40 seconds of ablation and 45 seconds of sample
388 washout and gas blank measurement. Dwell times were of 100 ms for ⁸⁵Rb, ⁸⁶Sr¹⁶O and
389 ⁸⁷Sr¹⁶O, 50 ms for ⁸⁶Sr and ⁸⁷(Sr+Rb), 20 ms for ⁸⁸Sr, ⁸⁸Sr¹⁶O and ⁸⁸Sr¹⁶OH, and 10 ms for
390 other elements (e.g., Ca, Ti, Ni, Ce, Yb, Th), which were monitored to assess potential
391 contamination by extraneous material. Data reduction was performed using the “Rb-Sr
392 isotopes” data reduction scheme in Iolite 4 (Paton et al., 2011). Instrumental drift and
393 quantification of ⁸⁷Sr/⁸⁶Sr and ‘uncorrected’ ⁸⁷Rb/⁸⁶Sr were undertaken by repeated ablation of
394 NIST610, which was measured every block of 15 unknowns including in-house mica standards
395 (see below). NIST610 is a synthetic glass with different ablation properties than mica and,
396 therefore, this approach provides biased (i.e. ‘uncorrected’) ⁸⁷Rb/⁸⁶Sr ratios in mica analyses
397 (e.g., Redaa et al., 2021). Correction of NIST610-based ‘uncorrected’ ⁸⁷Rb/⁸⁶Sr in the mica
398 unknowns was performed following the method outlined by Giuliani et al. (2024). The
399 calculated age of an in-house mica standard from the Wimbledon kimberlite (South Africa),
400 which has a robustly constrained Rb-Sr age of 114.5 ± 0.8 Ma (2σ s.d.) based on isotope
401 dilution analyses (Sarkar et al., 2023) and exhibits large variation in Rb/Sr (almost 3 orders of
402 magnitude), was employed to calculate a correction factor that is then employed to obtain the
403 final ⁸⁷Rb/⁸⁶Sr in the mica unknowns. The validity of this approach was confirmed by analyses
404 of micas from the Bultfontein kimberlite (South Africa) and Mount Dromedary monzonite
405 (MD-2; Australia) which returned Rb-Sr ages that are indistinguishable from solution-mode
406 Rb-Sr and Ar-Ar analyses of mica on the same sample: 88.3 ± 0.2 Ma (Fitzpayne et al., 2020),
407 and 99.20 ± 0.08 Ma (Phillips et al., 2017), respectively (**Supplementary Table S2**). Time-
408 resolved spectra of mica unknowns and reference materials were screened to remove
409 anomalous regions based on e.g., low concentrations of Rb and high concentrations of Sr, Ca,
410 Ce and/or other incompatible trace elements. Analyses with total signals of less than 10 seconds
411 (after screening) and with anomalously low contents of Rb or high contents of Sr (and Ca),
412 often resulting in ⁸⁷Rb/⁸⁶Sr < 2.5 , as well as analyses with large ⁸⁷Sr/⁸⁶Sr uncertainties and data
413 points that plotted distinctly off the isochron were not included in the Nicolaysen diagrams
414 (**Supplementary Table S3**). Trace element concentrations were not quantified.
415



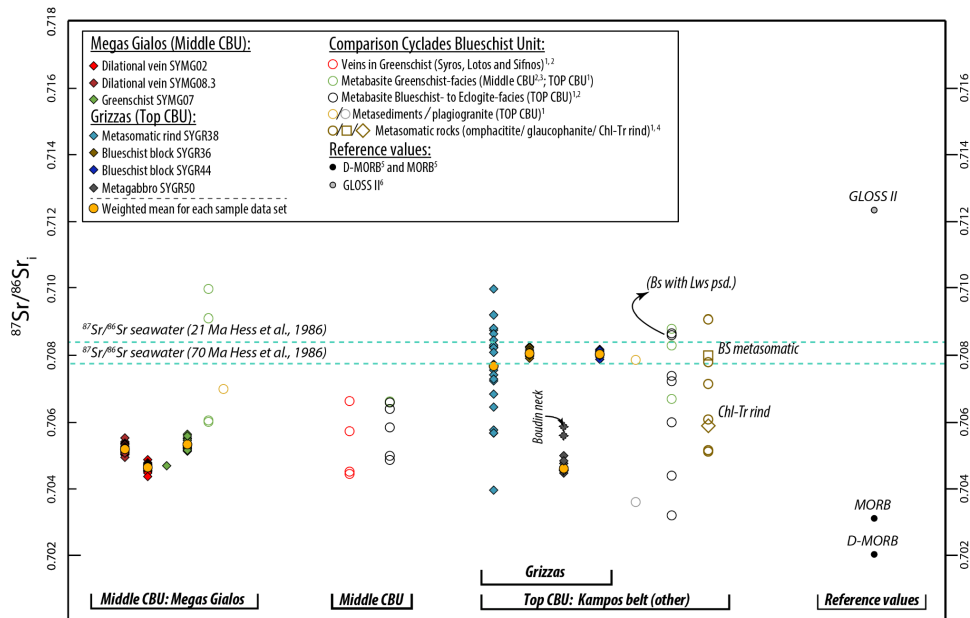
416 Results

417 Epidote Sr isotopes

418 $^{87}\text{Sr}/^{86}\text{Sr}$ ratios were measured by laser ablation MC-ICP-MS in 5 of the 10 samples employed
419 for mica Rb-Sr geochronology. Two additional samples (SYGR44; SYGR50) were also
420 included to corroborate the signature of the blueschist and metagabbro rocks. For comparison,
421 we also present isotope-dilution Sr isotope data in samples from the Megas Gialos locality,
422 including the 3 samples analyzed for epidote and mica Rb-Sr isotopes. A summary of the new
423 and available Sr isotope data for epidote is reported in **Figure 3** and the full datasets, including
424 bulk rock Sr and Nd isotopic compositions, are included in **Supplementary Tables S1 and**
425 **S4**.

426 At Grizzas (Kampos belt), the two blueschist samples (SYGR36 and 44) show very small
427 ranges in epidote $^{87}\text{Sr}/^{86}\text{Sr}$ compositions (see **Supplementary Figure S2**) with
428 indistinguishable weighted means of 0.70805 ± 0.00006 (2SE; $n = 12$) and 0.70802 ± 0.00005
429 (2SE; $n = 18$; **Table 2 and Supplementary Figure S2**). The other two Grizzas samples (the
430 metasomatic rind SYGR38 and the metagabbro SYGR50) exhibit larger isotopic variations.
431 $^{87}\text{Sr}/^{86}\text{Sr}$ in sample SYGR38 vary widely between 0.70426 ± 0.00008 and 0.710002 ± 0.00008
432 ($n = 22$) with no statistically distinct populations (**Figure 3**). The weighted mean (although
433 statistically meaningless) is similar to those of SYGR36 and SYGR44: 0.70767 ± 0.00058 . In
434 sample SYGR50, 16 epidote grains parallel to the foliation yield a restricted range in Sr isotope
435 values corresponding to a weighted mean of 0.70460 ± 0.00004 , which is substantially less
436 radiogenic than the blueschist samples from Grizzas, although similar to the lowest $^{87}\text{Sr}/^{86}\text{Sr}$
437 of sample SYGR38. Four epidote grains within boudin necks of sample SYGR50 show more
438 radiogenic values of up to 0.70585 ± 0.00020 .

439
440 Epidote in the three samples from Megas Gialos show very limited within-sample $^{87}\text{Sr}/^{86}\text{Sr}$
441 variability with weighted means of 0.70466 ± 0.00004 ($n = 24$) for SYMG02; $0.70534 \pm$
442 0.00005 ($n = 25$) for SYMG07 and 0.70520 ± 0.00005 ($n = 31$) for SYMG08.03. The epidote
443 Sr isotope compositions are not correlated with the lithology as the greenschist sample
444 SYMG07 has the same $^{87}\text{Sr}/^{86}\text{Sr}$ as one of the two dilatational veins (SYMG02 and 08.03).
445 Measured (i.e. present-day) $^{87}\text{Sr}/^{86}\text{Sr}$ of bulk rock SYMG07 is 0.705414 ± 0.000008 (2σ s.d. of
446 NBS987 standards measured in the same session), marginally more radiogenic than the
447 SYMG07 epidote, and minimally affected by radiogenic ingrowth (e.g., ~ 0.0002 in 50 Myr)
448 due to low bulk-rock $^{87}\text{Rb}/^{86}\text{Sr}$ of 0.290 (**Supplementary Table S1**). The bulk-rock $^{87}\text{Sr}/^{86}\text{Sr}$
449 of SYMG08.03 (0.705281 ± 0.000006) is almost indistinguishable from the epidote value
450 reported above. The very low $^{87}\text{Rb}/^{86}\text{Sr}$ (0.073) suggests minimal radiogenic Sr ingrowth in
451 this bulk sample.



453
 454 **Figure 3.** Overview of $^{87}\text{Sr}/^{86}\text{Sr}$ in-situ laser ablation MC-ICP-MS epidote data points and comparison to ID-
 455 TIMS (whole rock and multi-mineral) analyses from different localities in Syros. The resulting $^{87}\text{Sr}/^{86}\text{Sr}$ values
 456 are assumed to represent initial ratios due to the lack of Rb in epidote. For comparison, pristine MORB and D-
 457 MORB, as well as compiled trench filling sediments (GLOSS II) along with Cretaceous to Miocene $^{87}\text{Sr}/^{86}\text{Sr}$
 458 seawater values are shown. 1 – Glodny and Ring (2022); 2 – Kotowski et al. (2022); 3 – Bröcker et al. (2013); 4
 459 – Bröcker and Enders (2001); 5 – Salters and Stracke (2004); 6 – Plank (2014).

460 Mica Rb-Sr dating

461 In this section we report the mica Rb-Sr isotope data and describe the related isochronous array
 462 for each sample, complemented in 5 cases by epidote Sr isotope results. The complete white
 463 mica dataset, including Rb and Sr isotope ratios, is provided in **Supplementary Table S3** (see
 464 **Table 2** for a summary of the age data). For each sample we also provide a model age where
 465 the mica Rb/Sr isochron is anchored to an assumed $^{87}\text{Sr}/^{86}\text{Sr}$ value, that is 0.7080 ± 0.0005 for
 466 all the samples from Grizzas, and 0.7050 ± 0.0005 for those from Megas Gialos. For Grizzas,
 467 employing this value is justified by the fact that the weighted mean of epidote Sr isotopes are
 468 ~ 0.708 for three or the four analysed samples (**Figure 3**; see also the compiled data in **Figure**
 469 **3** for metabasites from the Top CBU), and “unanchored” mica Rb/Sr isochrons are generally
 470 within uncertainty of this value (see below). The epidote and bulk-rock compositions at Megas
 471 Gialos cluster at $^{87}\text{Sr}/^{86}\text{Sr}$ of ~ 0.705 (**Figure 3**) hence providing a robustly constrained initial
 472 Sr composition for anchoring the mica-based Nicolaysen arrays. In the discussion section we
 473 will address the impact of changing initial (or “common”) $^{87}\text{Sr}/^{86}\text{Sr}$ composition in the
 474 calculated Rb/Sr ages.



475 **SYGR36**

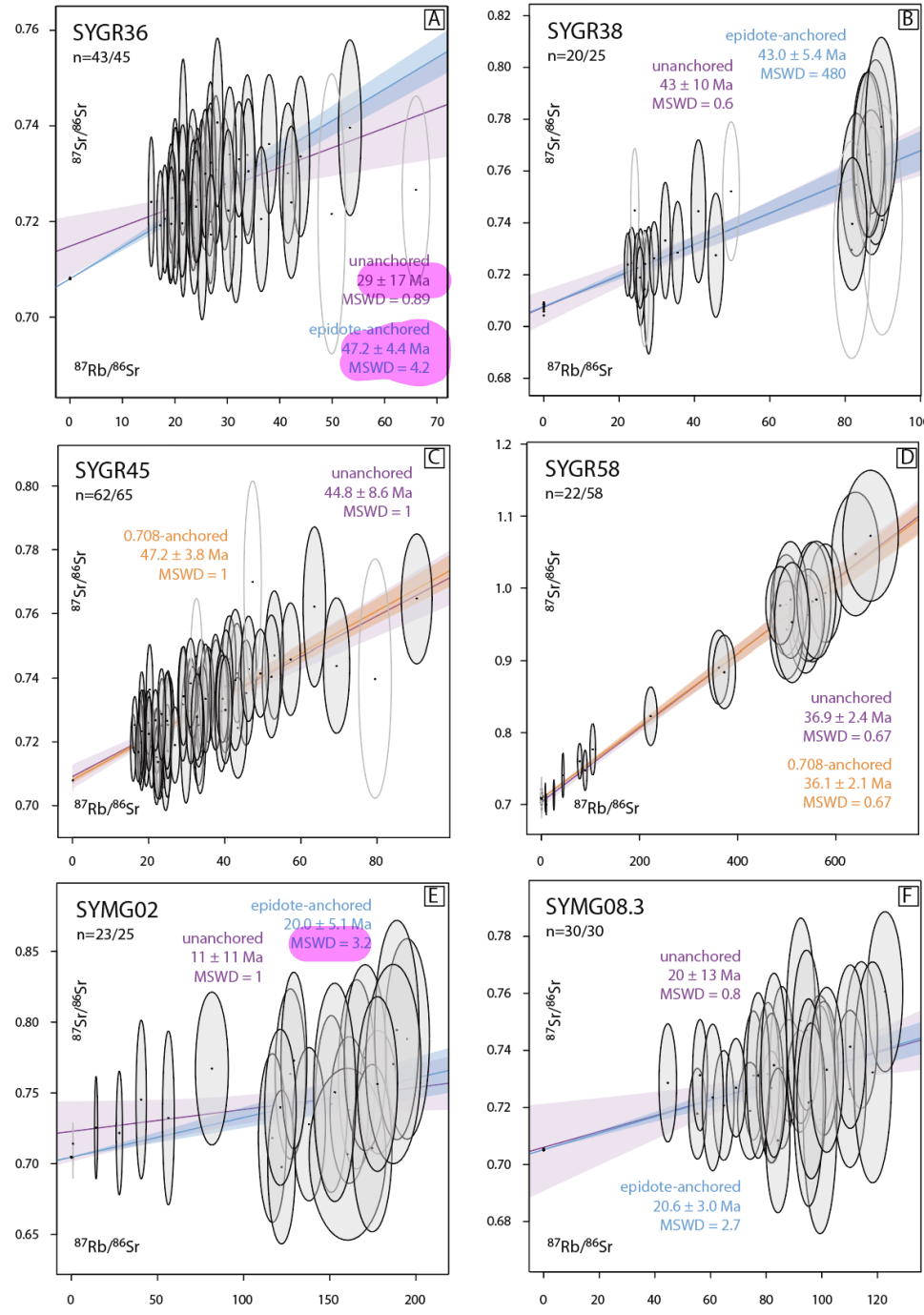
476 White mica in the blueschist block sample SYGR36 show a spread in $^{87}\text{Rb}/^{86}\text{Sr}$ between 15
477 and 53 ($n = 43/45$) associated with variations in $^{87}\text{Sr}/^{86}\text{Sr}$ between 0.7166 and 0.7407 (**Figure**
478 **4A**). The limited Rb/Sr spread results in a poorly defined “unanchored” isochron age of $29 \pm$
479 17 Ma (2 se , $\text{MSWD} = 0.89$, initial $^{87}\text{Sr}/^{86}\text{Sr} = 0.7149 \pm 0.0062$). Anchoring the phengite Rb-
480 Sr data to epidote from the same sample (weighted mean $^{87}\text{Sr}/^{86}\text{Sr} = 0.70805 \pm 0.00006$)
481 provides a rather different (although within uncertainty) and considerably more precise age of
482 47.2 ± 4.4 Ma (2s, $\text{MSWD} = 4.2$). Assuming a modeled initial $^{87}\text{Sr}/^{86}\text{Sr}$ of 0.7080 ± 0.0005 (1s)
483 provides an age of 46.9 ± 5.1 Ma (2s, $\text{MSWD} = 0.96$), overlapping closely with the epidote-
484 anchored isochron age.

485 **SYGR37**

486 White mica grains in the metasomatic rind sample SYGR37 show a slightly larger spread in
487 $^{87}\text{Rb}/^{86}\text{Sr}$ (22-112, $n = 36/38$) and $^{87}\text{Sr}/^{86}\text{Sr}$ (0.7211-0.7676) compared to SYGR36, resulting
488 in a more precise unanchored isochron age of 32.3 ± 7.5 Ma ($\text{MSWD} = 0.51$, initial $^{87}\text{Sr}/^{86}\text{Sr} =$
489 0.7158 ± 0.0059 ; **Supplementary Figure S3**). Anchoring these mica Rb-Sr to modeled initial
490 $^{87}\text{Sr}/^{86}\text{Sr}$ of 0.7080 ± 0.0005 yields an older age of 41.1 ± 3.1 Ma ($\text{MSWD} = 0.66$).

491 **SYGR38**

492 White mica in the metasomatic rind SYGR38 shows spreads between 22-90 and 0.7140-0.7771
493 for $^{87}\text{Rb}/^{86}\text{Sr}$ and $^{87}\text{Sr}/^{86}\text{Sr}$, respectively ($n = 20/25$, with 5 analyses excluded based on short
494 signals of less than 10 seconds). The corresponding unanchored isochron age is 43 ± 10 Ma
495 ($\text{MSWD} = 0.6$, initial $^{87}\text{Sr}/^{86}\text{Sr} = 0.7075 \pm 0.0064$; **Figure 4B**). Adding epidote Sr isotopes
496 (weighted mean $^{87}\text{Sr}/^{86}\text{Sr} = 0.70767 \pm 0.00058$) to the mica Rb-Sr isochron yields the same,
497 yet more precise age of 43.0 ± 5.4 Ma ($\text{MSWD} = 480$). Using a modeled initial $^{87}\text{Sr}/^{86}\text{Sr}$ of
498 0.7080 ± 0.0005 (1s) results in a similar age of 42.5 ± 5.5 Ma ($\text{MSWD} = 0.54$). Considering
499 the large spread in epidote $^{87}\text{Sr}/^{86}\text{Sr}$ values (~ 0.7043 to ~ 0.7100), we have also calculated
500 model ages using initial $^{87}\text{Sr}/^{86}\text{Sr}$ of 0.7050 and 0.7100 and these are within uncertainty of each
501 other: 46.5 ± 5.6 Ma ($\text{MSWD} = 0.57$) and 39.8 ± 5.5 Ma ($\text{MSWD} = 0.57$), respectively(
502 **Supplementary Figure S4**).



503
 504
 505
 506
 507

Figure 4. Representative laser-ablation ICP-MS/MS Rb-Sr isochrons of white micas from Grizzas (North East Syros Island, SYGR, A-D) and Megas Gialos (South Syros Island, SYMG, E-F). The size of the ellipses represents internal 2 SE (standard error), where data points that were excluded from the regression are displayed as empty ellipses. Isochronous regressions are plotted together with their 95% confidence level envelopes in different



508 colours based on the employed anchoring technique: purple for mica-only unanchored regressions; blue for
509 regressions anchored to epidote; orange for regressions anchored to a modelled initial $^{87}\text{Sr}/^{86}\text{Sr}$ of $0.7080 \pm$
510 0.0005 . The number below the sample labels indicates the number of mica analyses. All plots were generated
511 using IsoplotR (Vermeesch, 2018).

512

513 **SYGR41**

514 White mica from the dilational vein SYGR41 show a limited spread in $^{87}\text{Rb}/^{86}\text{Sr}$ between 14-
515 63 (n = 36/36) associated with variations in $^{87}\text{Sr}/^{86}\text{Sr}$ between 0.7116 and 0.7498. An
516 unanchored isochron through these data yields an age of 45 ± 11 Ma (MSWD = 0.78, initial
517 $^{87}\text{Sr}/^{86}\text{Sr} = 0.7076 \pm 0.0049$). Anchoring these mica Rb-Sr data to a modeled initial $^{87}\text{Sr}/^{86}\text{Sr}$ of
518 0.7080 ± 0.0005 (1s) yields the same, yet more precise age of 44.7 ± 4.5 Ma (2s, MSWD =
519 0.74).

520

521 **SYGR42**

522 $^{87}\text{Rb}/^{86}\text{Sr}$ and $^{87}\text{Sr}/^{86}\text{Sr}$ ratios in phengites from the metasomatized metagabbro sample
523 SYGR42 range from 27 to 185 and 0.7155 to 0.8162, respectively (n = 30/30), and the
524 corresponding unanchored isochrons provides an age of 46 ± 9 Ma (MSWD = 1.3, initial
525 $^{87}\text{Sr}/^{86}\text{Sr} = 0.7090 \pm 0.0079$). Anchoring these mica Rb-Sr data to $^{87}\text{Sr}/^{86}\text{Sr} = 0.7080 \pm 0.0005$
526 (1s) results in an overlapping, although more precise age of 46.6 ± 4.6 Ma (MSWD = 1.2).

527

528 **SYGR45**

529 Two generations of phengite laths, parallel and oblique to the main foliation, from the
530 metasedimentary rock sample SYGR45 display $^{87}\text{Rb}/^{86}\text{Sr}$ values between 16 and 90 (n = 62/65)
531 and a corresponding variation in $^{87}\text{Sr}/^{86}\text{Sr}$ between 0.7134 and 0.7647, with no systematic
532 difference between the two textural types of mica (**Figure 4C; Supplementary Table S3**). The
533 resulting unanchored isochron has a slope equivalent to an age of 44.8 ± 8.6 Ma (MSWD = 1,
534 initial $^{87}\text{Sr}/^{86}\text{Sr} = 0.7092 \pm 0.0038$). Anchoring these mica Rb/Sr data to a modeled initial
535 $^{87}\text{Sr}/^{86}\text{Sr}$ of 0.7080 ± 0.0005 (1s) yields a slightly older and more precise age of 47.2 ± 3.8 Ma
536 (MSWD = 1), overlapping with the unanchored age within uncertainty. Using a more
537 radiogenic initial $^{87}\text{Sr}/^{86}\text{Sr}$ of 0.7100 has a small effect on the calculated age (43.2 ± 3.8 ;
538 MSWD = 1).

539

540 **SYGR58**

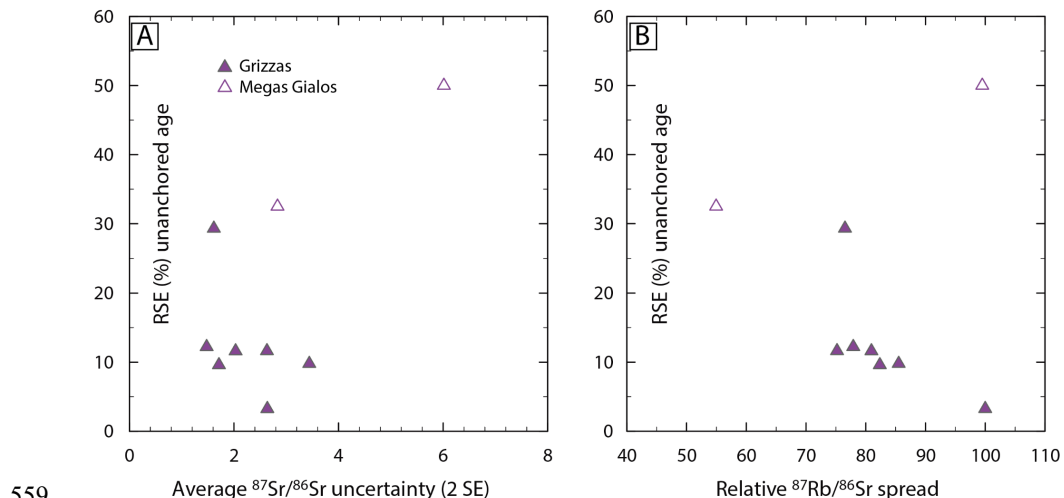
541 The two textural types of white mica identified in the felsic pod sample SYGR58, parallel and
542 oblique to the main foliation, exhibit indistinguishable Rb-Sr isotope systematics
543 (**Supplementary Table S3**) and are, hence, described together. These white micas show the
544 largest Rb/Sr spread observed in the sample set of between 8 and 671 (n = 22/58, where only
545 analyzes with $^{87}\text{Rb}/^{86}\text{Sr} > 2.5$ were considered for the isochron), which is consistent with the
546 felsic nature of this sample. The spread in $^{87}\text{Sr}/^{86}\text{Sr}$ is between 0.670 and 1.073, resulting in
547 precise, although unanchored Rb/Sr age of 36.9 ± 2.4 Ma (MSWD = 0.67, initial $^{87}\text{Sr}/^{86}\text{Sr} =$



548 0.7038 ± 0.0072; **Figure 4D**). Anchoring these mica Rb/Sr data to a modeled initial $^{87}\text{Sr}/^{86}\text{Sr}$
549 of 0.7080 ± 0.0005 (1s) yields a similar age of 36.1 ± 2.1 Ma (2s, MSWD = 0.67).
550

551 SYMG02

552 Phengites from the dilational vein sample SYMG02 show a relatively large $^{87}\text{Rb}/^{86}\text{Sr}$ spread
553 between 14 and 195 (n = 23/25) associated with a restricted $^{87}\text{Sr}/^{86}\text{Sr}$ spread between 0.6976
554 and 0.7944. These data define a meaningless unanchored isochron (age = 11 ± 11 Ma, MSWD
555 = 1, initial $^{87}\text{Sr}/^{86}\text{Sr}$ = 0.723 ± 0.021; **Figure 4E**). Adding epidote Sr data from the same sample
556 (weighted mean $^{87}\text{Sr}/^{86}\text{Sr}$ = 0.70466 ± 0.00004) to the mica Rb-Sr isotopes results in a more
557 meaningful age of 20.0 ± 5.1 Ma (MSWD = 3.2). Using a modeled initial $^{87}\text{Sr}/^{86}\text{Sr}$ anchor of
558 0.7050 ± 0.0005 (1s) yields a similar age of 19.8 ± 5.2 Ma (2s, MSWD = 1).



559
560 **Figure 5.** Comparison of relative standard deviations (1 SE, standard error) of unanchored mica Rb/Sr ages and
561 (A) average $^{87}\text{Sr}/^{86}\text{Sr}$ uncertainties and (B) relative (%) $^{87}\text{Rb}/^{86}\text{Sr}$ spread. The latter was defined as the ratio
562 between the absolute $^{87}\text{Rb}/^{86}\text{Sr}$ spread and the highest $^{87}\text{Rb}/^{86}\text{Sr}$ value observed for any given sample, resulting in
563 a number between 0 and 100%.

564 SYMG07

565 $^{87}\text{Rb}/^{86}\text{Sr}$ and $^{87}\text{Sr}/^{86}\text{Sr}$ values in white mica from the greenschist sample SYMG07 vary
566 between 75-231 and 0.7199-0.8121, respectively (n = 12/13), yielding a meaningless isochron
567 age of 6.1 ± 31.2 Ma (MSWD = 1.2, initial $^{87}\text{Sr}/^{86}\text{Sr}$ = 0.749 ± 0.063; **Supplementary Figure**
568 **S3**). Coupling white mica with the SYMG07 epidote data (weighted mean $^{87}\text{Sr}/^{86}\text{Sr}$ = 0.70534
569 ± 0.00005) results in an age of 27.1 ± 8.4 Ma (MSWD = 3.4). An identical age is obtained
570 using a model initial $^{87}\text{Sr}/^{86}\text{Sr}$ of 0.7050 ± 0.0005 (1s): 27.4 ± 8.4 Ma (2s, MSWD = 1.2).
571



572 SYMG08

573 Phengites from dilational vein SYMG08.3 show a spread in $^{87}\text{Rb}/^{86}\text{Sr}$ between 45 and 123 (n
 574 = 30/30) associated with variations in $^{87}\text{Sr}/^{86}\text{Sr}$ between 0.7084 and 0.7606 (**Figure 4F**). These
 575 data define an unanchored isochron age of 20 ± 13 Ma (MSWD = 0.8, initial $^{87}\text{Sr}/^{86}\text{Sr} = 0.706$
 576 ± 0.015). Adding Sr epidote data (weighted mean $^{87}\text{Sr}/^{86}\text{Sr} = 0.70520 \pm 0.00005$) to the
 577 phengite Rb/Sr data results in the same, yet more precise age of 20.6 ± 3.0 Ma (MSWD = 2.7).
 578 The results hardly change by anchoring the mica Rb/Sr data to a modeled initial $^{87}\text{Sr}/^{86}\text{Sr}$ of
 579 0.7050 ± 0.0005 (1s): 20.8 ± 3.1 Ma (MSWD = 0.75) (**Supplementary Figure S4**).

Table 2. Summary of epidote Sr isotopes and mica Rb-Sr ages

Sample ID	Epidote $^{87}\text{Sr}/^{86}\text{Sr}$ *			Mica analyses			Mica age, unanchored **			Mica + epidote age (Ma)			Mica age (Ma), anchored ***		
	n	mean	2 SE	n	age (Ma)	2 SE	MSWD	isochron y intercept	age (Ma)	2 SE	MSWD	age (Ma)	2 SE	MSWD	
<i>Grizzas (NE Syros)</i>															
SYGR36	12	0.70805	0.00006	43/45	29	17	0.89	0.7149 ± 0.0062	47.2	4.4	4.2	46.9	5.1	0.96	
SYGR37	—	—	—	36/38	32.3	7.5	0.51	0.7158 ± 0.0059	—	—	—	41.1	3.1	0.66	
SYGR38	21	0.70767	0.00058	20/25	43	10	0.60	0.7075 ± 0.0064	43.0	5.4	480	42.5	5.5	0.54	
SYGR41	—	—	—	36/36	45	11	0.78	0.7076 ± 0.0049	—	—	—	44.7	4.5	0.74	
SYGR42	—	—	—	30/30	46	9	1.30	0.7090 ± 0.0079	—	—	—	46.6	4.6	1.2	
SYGR44	18	0.70802	0.00005	—	—	—	—	—	—	—	—	—	—	—	
SYGR45	—	—	—	62/65	44.8	8.6	1.00	0.7092 ± 0.0038	—	—	—	47.2	3.8	1	
SYGR50	16	0.70460	0.00004	—	—	—	—	—	—	—	—	—	—	—	
SYGR58	—	—	—	22/58	36.9	2.4	0.67	0.7038 ± 0.0072	—	—	—	36.1	2.1	0.67	
<i>Megas Gialos (SE Syros)</i>															
SYMG02	24	0.70466	0.00004	23/25	11	11	1.00	0.723 ± 0.021	20.0	5.1	3.2	19.8	5.2	1	
SYMG07	25	0.70534	0.00005	12/13	6.4	31.2	1.20	0.749 ± 0.063	27.1	8.4	3.4	27.4	8.4	1.2	
SYMG08.3	31	0.70520	0.00005	30/30	20	13	0.80	0.706 ± 0.015	20.6	3.0	2.7	20.8	3.1	0.75	

* laser ablation, multi-collector ICP-MS; complete dataset in Supplementary Table S1

** laser ablation, ICP-MS/MS; complete dataset in Supplementary Table S3

*** anchoring values: 0.7080 ± 0.0005 for SYGR samples; 0.7050 ± 0.0005 for SYMG samples

580

581 Discussion

582 Optimal strategies to obtain robust Rb-Sr ages for white 583 mica in young metamorphic rocks by LA-ICP-MS/MS

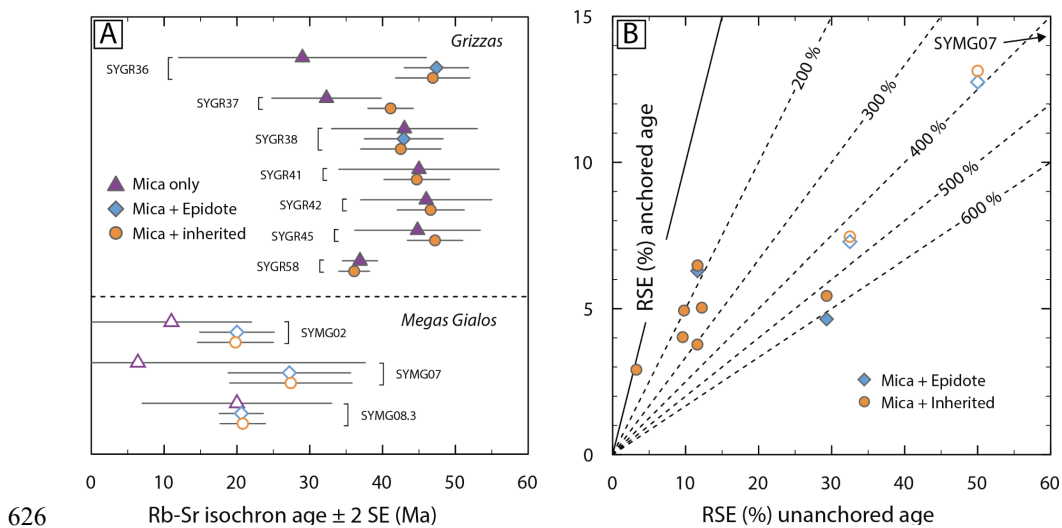
584 White mica in all the investigated samples, and regardless of their bulk-rock chemistry (i.e.
 585 mafic and metasomatic), exhibit limited spread in Rb/Sr compared to previous studies (e.g.,
 586 Kirkland et al., 2023, Glodny and Ring 2022). Except for the relatively large spread observed
 587 in the felsic sample SYGR58 ($^{87}\text{Rb}/^{86}\text{Sr} = 8$ to 671), the Rb/Sr range of all the other samples
 588 never exceeds one order of magnitude and in some cases less (e.g., $^{87}\text{Rb}/^{86}\text{Sr} = 15$ -53 in
 589 blueschist SYGR36) compared to, for example, the two to three orders of magnitude in
 590 phlogopite from lamproites and kimberlites (Giuliani et al., 2024), or biotite in some
 591 metamorphosed granites (Ceccato et al., 2024). In addition, the combination of relatively low
 592 Rb contents (not quantified but inferred from low Rb/Sr ratios) and geologically young
 593 (Cenozoic) age of the Syros micas did not allow the ingrowth of substantial radiogenic ^{87}Sr as
 594 shown by the low measured $^{87}\text{Sr}/^{86}\text{Sr}$ (generally <0.8 ; **Supplementary Table S3**). Low ^{87}Sr
 595 contents are associated with large uncertainties for $^{87}\text{Sr}/^{86}\text{Sr}$, which systematically exceed 1%
 596 (2SE) for individual measurements (**Figure 5A**). The compounded effects of low absolute
 597 $^{87}\text{Rb}/^{86}\text{Sr}$ values (generally <200 and, for some samples, <100), limited spread in Rb/Sr and
 598 poor precision in the quantification of $^{87}\text{Sr}/^{86}\text{Sr}$ result in large uncertainties associated with the
 599 slopes of unanchored mica Rb-Sr isochrons. These uncertainties translate to a poor precision



for the related ages with 10-29 %RSE (relative standard error) in the SYGR samples (except for the felsic sample SYGR58, with an RSE of 3%, i.e. 36.9 ± 2.4 Ma, 2SE), and even larger for the younger SYMG samples (**Figure 6A**). The inverse correlation between relative $^{87}\text{Rb}/^{86}\text{Sr}$ spread and age uncertainty of unanchored isochrons in **Figure 5B** exemplifies the impact of Rb/Sr variations on age precision. In at least three cases (SYGR36, SYMG02 and SYMG07) these unanchored mica-only isochronous arrays are not just imprecise, but also rather inaccurate as shown by the substantially older ages of the mica + epidote isochron for SYGR36 (29 ± 17 Ma vs 47.2 ± 4.4 Ma for SYGR36) or simply geologically meaningless (11 ± 11 Ma and 6.4 ± 31 Ma for SYMG02 and SYMG07, respectively; **Table 2**).

609

To overcome the limitations in mica Rb-Sr geochronology by LA-ICP-MS/MS due to low Rb/Sr and/or young ages, the two viable solutions explored here include anchoring the isochronous arrays to either the Sr isotope composition of a low Rb/Sr phase in textural (and probably chemical equilibrium) with mica, such as epidote, or an assumed $^{87}\text{Sr}/^{86}\text{Sr}$ value. The latter approach effectively provides a “model age” and, while previously explored by Rösel and Zack (2021), it is rigorously evaluated herein by a systematic comparison with initial Sr isotope constraints from epidote and bulk rocks. Anchoring mica isochrons to a low Rb/Sr phase has been rarely applied in mica Rb/Sr geochronology by LA-ICP-MS/MS (Barnes et al., 2024; Giuliani et al., 2024), while being widely employed for conventional Rb/Sr dating by isotope dilution (e.g., Maas, 2003; Glodny et al., 2008; Hyppolito et al., 2016; Angiboust et al., 2018; Dalton et al., 2020). Comparisons of unanchored mica Rb/Sr ages with those anchored using mean $^{87}\text{Sr}/^{86}\text{Sr}$ of epidote analyses show an improvement in precision of up to 6 times (**Figure 6B**) – as well as better accuracy in some cases as shown above for SYGR36. Clearly, in young high-pressure metamorphic rocks such as those from Syros, this approach is recommended to obtain robust age constraints even when the limited spread in mica Rb/Sr prevents generation of meaningful isochronous arrays (i.e. SYMG02 and 07).



626
 627 **Figure 6.** (A) Overview of mica Rb-Sr ages using mica datapoints only (unanchored isochrons, purple), anchoring
 628 to epidote (blue) and anchoring to an assumed initial $^{87}\text{Sr}/^{86}\text{Sr}$ composition (orange). Initial $^{87}\text{Sr}/^{86}\text{Sr}$ was assumed



629 to be 0.7080 ± 0.0005 for Grizzas and 0.7050 ± 0.0005 for Megas Gialos (see text). (B) Comparison of the
630 uncertainties expressed as % RSE (relative standard error) for unanchored mica-only ages and ages anchored to
631 either epidote or an assumed initial $^{87}\text{Sr}/^{86}\text{Sr}$. Samples from Grizzas and Megas Gialos are shown as empty and
632 full symbols, respectively. Location of Megas Gialos sample SYMG07 (unanchored age 6.4 ± 31 Ma, 243% RSE)
633 is shown with an arrow..

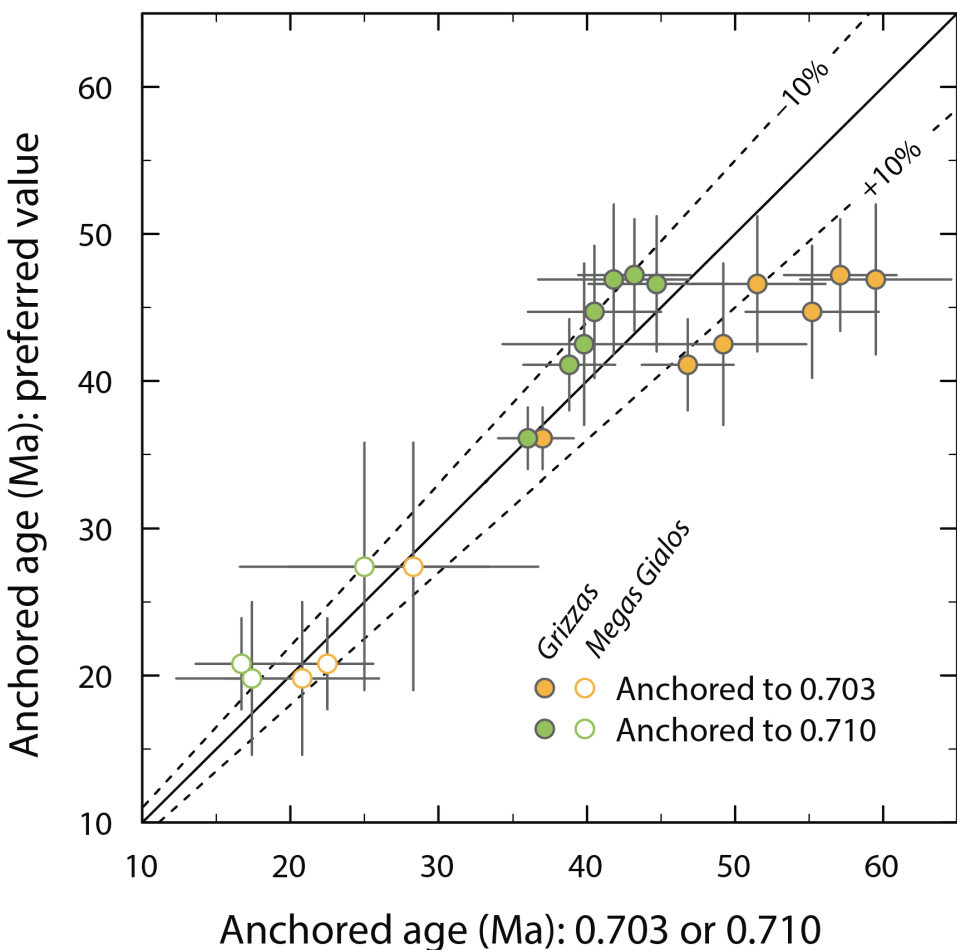
634 Model ages are also, not surprisingly, substantially more precise than unanchored mica-only
635 Rb/Sr ages. However, their accuracy deserves scrutiny. Where epidote data are available, the
636 model ages calculated in this work can be employed to show the effect of inaccurate initial
637 $^{87}\text{Sr}/^{86}\text{Sr}$ in the isochron ages (**Figure 7**). At Grizzas, epidote $^{87}\text{Sr}/^{86}\text{Sr}$ varies between 0.7043
638 and 0.7100 (all this variation is contained in the metasomatic rind sample SYGR38). Using
639 available bulk rock data for the Kambos Belt (**Figure 3**), this range can be extended downward
640 to ~ 0.7030 , hence effectively bracketing the possible compositions of initial Sr to calculate
641 mica model ages. For simplicity, the same range is employed for Megas Gialos. Beyond the
642 model ages presented in the results section and **Table 2**, for each sample two additional model
643 ages are calculated using an initial $^{87}\text{Sr}/^{86}\text{Sr}$ of 0.7030 ± 0.0005 and 0.7100 ± 0.0005 , respectively
644 (**Figure 7 and Supplementary Table S5**). In the Grizzas samples, using an initial $^{87}\text{Sr}/^{86}\text{Sr}$ of
645 0.7100 generates model ages that are generally within uncertainty of those where the initial
646 $^{87}\text{Sr}/^{86}\text{Sr}$ was assumed to be 0.7080; conversely, the ages are $\geq 10\%$ older
647 if an initial $^{87}\text{Sr}/^{86}\text{Sr}$ value of 0.7030 is employed. **Figure 7** shows that the older the
648 sample, the more dramatic is the impact of the initial $^{87}\text{Sr}/^{86}\text{Sr}$ chosen. For the > 40 Ma Grizzas
649 micas, the use of initial $^{87}\text{Sr}/^{86}\text{Sr}$ of 0.7100 provides ages that are resolvable (i.e. outside 2SE)
650 from those obtained employing 0.7030 as the initial $^{87}\text{Sr}/^{86}\text{Sr}$ ratio. Conversely, for the younger
651 (< 30 Ma) Megas Gialos samples, all the calculated model ages are within uncertainty of each
652 other. While the favored approach remains to analyze a low Rb/Sr phase cogenetic to mica
653 (e.g., epidote, plagioclase, carbonate, apatite), where there is limited independent knowledge
654 of initial Sr isotope compositions, we recommend employing $^{87}\text{Sr}/^{86}\text{Sr}$ that are intermediate
655 between those of likely endmembers representative of the examined lithologies.
656

657 At Grizzas, the blueschist blocks (samples SYGR36 and SYGR44) and a metasomatic rind
658 (sample SYGR38) consistently yielded initial $^{87}\text{Sr}/^{86}\text{Sr}$ values close to 0.708, although the latter
659 shows scattering between 0.704 to 0.710 (**Figure 3**). In the literature, highly radiogenic values
660 in metamafic and metasomatic rocks are common in the Kambos Belt, including for some
661 metasedimentary rocks (**Figure 3**). On the other hand, a metagabbro (sample SYGR50) yielded
662 an initial $^{87}\text{Sr}/^{86}\text{Sr}$ value close to 0.705. Similarly, the metamafic greenschist (SYMG07) and
663 veins (SYMG02 and SYMG08.3), along with additional vein and greenschist samples analyzed
664 for bulk rock $^{87}\text{Sr}/^{86}\text{Sr}$ only from Megas Gialos consistently yielded in-situ epidote and age-
665 corrected TIMS whole rock $^{87}\text{Sr}/^{86}\text{Sr}$ values of c. 0.705 (**Figure 3 and supplementary Table**
666 **S4**). We interpret the least radiogenic values to represent the oceanic magmatic protolith (e.g.,
667 Taylor and Lasaga, 1999) as well as veins that have equilibrated with or sourced from
668 metamafic rocks. In contrast, the more radiogenic signature could have been introduced by pre-
669 subduction seafloor alteration (Voigt et al., 2021), or by metasomatism by highly radiogenic
670 fluids for example derived from dehydration of metasedimentary rocks (Halama et al., 2011).
671 The latter hypothesis is more consistent with the spatial association between metasedimentary



672 and metasomatic rocks within the Grizzas shear zone. Our results demonstrate that for high-
673 pressure metasomatic rocks in subduction zones, the commonly assumed MORB-like $^{87}\text{Sr}/^{86}\text{Sr}$
674 value of 0.703 (Rösell and Zack, 2021) might not necessarily be representative of the initial Sr
675 isotope composition.

676



677

678 **Figure 7.** Covariation plots showing the effect of assumed initial $^{87}\text{Sr}/^{86}\text{Sr}$ on the mica Rb-Sr "model" age.
679 Preferred anchoring values are 0.7080 ± 0.0005 for Grizzas and 0.7050 ± 0.0005 for Megas Gialos (vertical
680 axis), which are compared to the extreme values in the range of observed bulk rock data for the Kambos Belt:
681 0.7030 ± 0.0005 (orange) and 0.7100 ± 0.0005 (green) (horizontal axis).

682 Application to Syros

683 To further validate our newly acquired mica Rb/Sr ages (anchored to epidote or, when not
684 available, to a modeled initial $^{87}\text{Sr}/^{86}\text{Sr}$; **Table 2**), we compare them with published age
685 constraints from Kambos Belt (Top CBU) and Middle CBU localities (**Figure 8**). Kotowski et
686 al. (2022) and Glodny and Ring (2022) compiled and reported new ID TIMS Rb-Sr ages,



687 mostly from the Western Kampos Belt and outcrops along the Top CBU in Syros, ranging from
688 53 to 43 Ma. This age range is interpreted to date the eclogite-to-blueschist-facies subduction
689 fabrics, developed during the prograde-to-peak-pressure and earliest stage of exhumation.
690 Robust U-Pb zircon and Lu-Hf garnet ages between 53 and 48 Ma constrain the peak
691 metamorphism in the Grizzas area (see Tomascheck et al., 2003; Lagos et al., 2007), and are
692 in agreement with the higher end of the Rb-Sr multi-mineral isochron ages including white
693 mica separates (e.g., Glodny and Ring 2022). Recent in-situ Rb-Sr dating of white mica also
694 showed an age of 48.4 ± 3.6 Ma for an eclogite from the Kathergaki cape (presumably
695 belonging to the Top CBU), which was also interpreted to date the near-peak metamorphism
696 (Barnes et al., 2024). At Grizzas, a blueschist block (SYGR36), a metasomatized metagabbro
697 (SYGR42) and a metasediment (SYGR45) yielded mica Rb/Sr ages ranging from 46.6 ± 4.6
698 Ma to 47.2 ± 3.8 Ma (Table 2 and Figure 6). Similarly, the dilatational vein sample SYGR41
699 returned a mica Rb/Sr age consistent with the HP metamorphic stage (44.7 ± 4.5 Ma). These
700 ages overlap with the low-end of the HP eclogite-to-blueschist-facies near-peak metamorphism
701 (peak to the earliest exhumation). Thus, and in line with previous investigations, the obtained
702 ages are interpreted to date near-peak metamorphism (for the blueschist SYGR36 and
703 metasediment SYGR45 samples) as well as the oldest record of near-peak metasomatism and
704 shear zone development leading to veining (SYGR41) and metagabbro fluid-assisted
705 deformation (SYGR42).

706

707 Kotowski et al. (2022) and Glodny and Ring (2022) noted that ages for the retrograde stage
708 associated with early decompression in the epidote blueschist-facies are in the 45 to 40 Ma
709 range, which could also be related to a mixed signal due to partial re-equilibration between the
710 early lawsonite blueschist- and HP greenschist-facies metamorphism (Glodny and Ring, 2022).
711 Blueschist- to (HP)greenschist-facies retrogression during exhumation is constrained to occur
712 between 40 and 20 Ma in the Kampos Belt based on previous Rb-Sr and Ar-Ar geochronology
713 (Glodny and Ring, 2022; Kotowski et al., 2022; Laurent et al., 2017). The metasomatic rind
714 samples SYGR37 and SYGR38 yielded mica Rb/Sr ages more consistent with fluid
715 metasomatism during the early exhumation stage in the epidote blueschist-facies stability field
716 (41.1 ± 3.1 Ma and 43.0 ± 5.4 Ma), although sample SYGR38 could be similarly interpreted to
717 date the metasomatism at near-peak pressure conditions considering the age uncertainty. These
718 c. 43 and 41 Ma ages date continuous fluid-rock interaction during HP deformation, which
719 preferentially occurs along shear zones (Zack and John, 2007; Angiboust et al., 2014; Kleine
720 et al., 2014; Smit and Pogge von Strandmann, 2020; Rajič et al., 2024). Only one sample (felsic
721 pod SYGR58) shows a statistically younger age of 36.1 ± 2.1 Ma, which is within the period
722 of exhumation and transition from blueschist to HP greenschist-facies. This age is consistent
723 with petrographic evidence of chlorite pseudomorphs after garnet suggestive of selective
724 greenschist-facies retrogression.

725 Overall, our near-peak ages align with two ages (samples 9C and 27; see Figure 8) reported
726 by Gyomlai et al. (2023a) for metasomatic lithologies within the Kampos Belt (Lia side), while
727 our HP early exhumation ages are comparable, within uncertainty, to one of their ages (sample
728 9A) – however, the significantly larger uncertainties of their mica Rb/Sr ages for similar rock
729 types should be noted. Additionally, Gyomlai et al. (2023a) obtained three ages of c. 36 Ma
730 (samples Ln57, Ln10 and Ln1), overlapping with our sample SYGR58 (felsic pod), which they



731 interpreted as retrograde ages dating the “main” metasomatic event along Kampos. Our data
732 points to at least one event of HP metasomatism within the range of 47.2 ± 3.8 Ma to $41.1 \pm$
733 3.1 Ma, however, due to method uncertainties, distinguishing between multiple events within
734 this time range is not feasible. Furthermore, Barnes et al. (2024) reported an in-situ white mica
735 Rb-Sr age of 44.5 ± 3.1 Ma for a metasomatic eclogite (Delfini locality; presumably Middle
736 CUB). Thus, our data, along with the results from Barnes et al. (2024) are at odds with previous
737 interpretations which suggested that metasomatism along the entire Kampos Belt occurred as
738 a discrete pulse during the latest stages of exhumation (Gyomlai et al., 2023a). Instead, we
739 suggest that metasomatism along Kampos initiated at near-peak metamorphic conditions and
740 evolved through HP early exhumation. This enables us to constrain localized shear zone
741 activity under HP conditions within the subduction channel in the presence of fluids. These
742 metasomatic events may be temporally and spatially associated with processes such as deep
743 slicing, underplating, and slow slip and tremor (Angiboust et al., 2012; Behr et al. 2018; Agard
744 et al., 2018; Muñoz-Montecinos et al., 2020; Tewksbury-Christle et a., 2021; Behr and
745 Bürgmann, 2021).

746

747 In the Megas Gialos locality, the host greenschist sample yielded an age of 27.4 ± 8.4 Ma, in
748 line with previous investigations of lithologies from the Middle CBU which have shown ages
749 of greenschist-facies metamorphism younger than c. 35 Ma using Ar-Ar and ID TIMS Rb-Sr
750 geochronology (Glodny and Ring, 2022; Bröcker et al., 2013). The vein samples SYMG02 and
751 SYMG08.3 yielded potentially younger (although not statistically resolvable) ages of $19.8 \pm$
752 5.2 Ma and 20.8 ± 3.1 Ma, interpreted to date dilatational veining during the latest stages of
753 exhumation of the metamorphic nappe at the base of the forearc (Cisneros et al., 2020; Muñoz-
754 Montecinos and Behr, 2023). These ages align with phengite + glaucophane veins from the
755 Top CBU unit (Elvia Island), which yielded virtually identical in-situ white mica Rb/Sr
756 (anchored to glaucophane) ages for dilatational veining at conditions of c. 350 °C and 0.8 GP
757 (Ducharme et al., 2024). Thus, the finding of similar ages for transitional blueschist-to-
758 greenschist-facies dilatational veining in Syros and in Evia Island demonstrates that across-dip
759 fluid flow toward the forearc is was ubiquitous process that occurred along the Hellenic
760 subduction zone at c. 20-22 Ma.

761

762

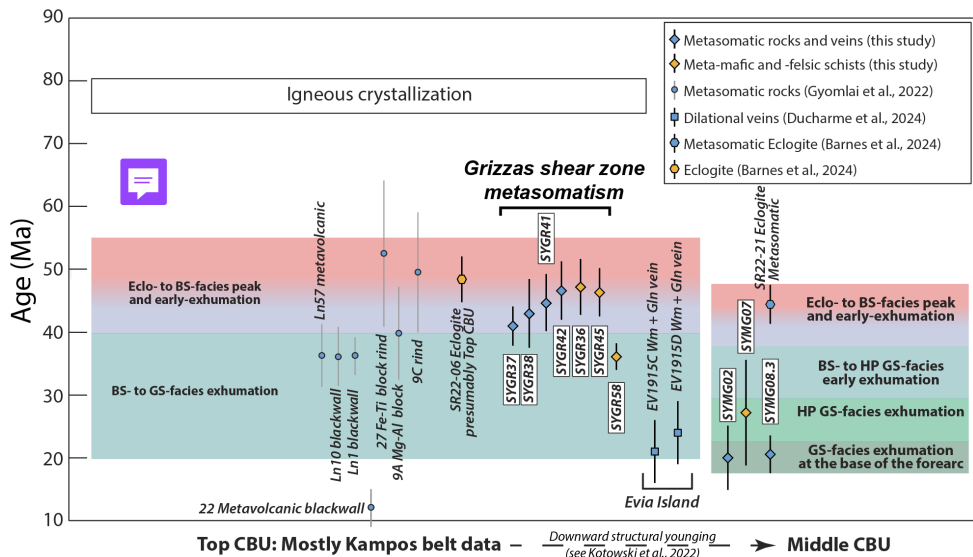


Figure 8. Summary of in-situ mica Rb-Sr ages from this study along with previous investigations in Syros Island and other localities along the CBU (Evia Island). The fields depicting the timing of the main tectonometamorphic events represents a synthesis of the compilations from Kotowski et al. (2022) and Glodny and Ring (2022), to which the reader is referred for a more complete compilation of the geochronologic data collected in Syros and all along the CBU. BS – blueschist; Eclo – eclogite; GS – greenschist; HP – high pressure.

769 Summary

770 We systematically evaluated the limitations of mica Rb-Sr dating by LA-ICP-MS/MS for
 771 young metamorphic samples using metamorphic rocks from Syros and attempted to circumvent
 772 these limitations by anchoring the initial $^{87}\text{Sr}/^{86}\text{Sr}$ component to either a low $^{87}\text{Rb}/^{86}\text{Sr}$ phase
 773 (i.e. epidote) or a modeled value. White mica analysis yielded narrow $^{87}\text{Rb}/^{86}\text{Sr}$ spread (ranging
 774 from 14 to 231 across the whole dataset), along with unradiogenic and imprecise $^{87}\text{Sr}/^{86}\text{Sr}$
 775 (generally <0.8 ; 2SE typically exceeding 1%). The combined effect of low $^{87}\text{Rb}/^{86}\text{Sr}$ values,
 776 limited spread in Rb/Sr and high uncertainty in $^{87}\text{Sr}/^{86}\text{Sr}$ resulted in mica-only ages (i.e. without
 777 anchoring) with very large uncertainties of 10 to 35% RSE or higher in some cases.

778 By anchoring these data to a low Rb/Sr phase such as epidote, age precision improved by up
 779 to six times, aligning with previous Rb-Sr TIMS data from Syros and other localities along the
 780 Cyclades blueschists unit. A first set of samples yielded ages consistent with near-peak to early
 781 exhumation along the epidote-blueschist-facies. The youngest ages likely date the latest stage
 782 of (HP)greenschist-facies exhumation. These ages are interpreted as dating various
 783 metasomatic stages that likely initiated at near-peak metamorphic conditions and continued
 784 during exhumation. We noted unexpectedly high radiogenic $^{87}\text{Sr}/^{86}\text{Sr}$ values and sometimes
 785 variability for the metamorphic-metasomatic materials. These values, likely resulting from
 786 focused fluid flow and metasomatism along the studied shear zone, underscore the importance
 787



788 of carefully selecting and evaluating the geologic context of $^{87}\text{Sr}/^{86}\text{Sr}$ anchors for future
789 applications of this “model” Rb-Sr white mica dating methodology.
790

791 **Data availability**

792 All Laser Ablation ICP-MS/MS and MC-ICP-MS data is available in the supplementary
793 material.

794 **Author contribution**

795 JM-M and AG designed the study and performed the experiments, with contributions from
796 BP. JM-M and WB collected the studied samples. AG and SO developed the statistical
797 analysis. JM-M and AG prepared the manuscript with contributions from all co-authors.

798 **Competing interests**

799 The authors declare that they have no conflict of interest.

800 **Acknowledgments**

801 We would like to thank Madalina Jaggi and Marcel Guillong for invaluable technical support
802 and Heather Stoll for granting access to the Agilent 8800 employed in this work. This project
803 was supported by the Swiss National Foundation (Ambizione fellowship n. PZ00P2_180126/1
804 to A. Giuliani) and ERC Starting Grant (947659) awarded to W.M. Behr.
805
806
807
808
809
810
811
812
813
814



815 References

- 816 1. Agard, P., Plunder, A., Angiboust, S., Bonnet, G., & Ruh, J. (2018). The subduction
817 plate interface: Rock record and mechanical coupling (from long to short timescales).
818 *Lithos*, 320, 537-566.
- 819 2. Angiboust, S., Wolf, S., Burov, E., Agard, P., & Yamato, P. (2012). Effect of fluid
820 circulation on subduction interface tectonic processes: Insights from thermo-
821 mechanical numerical modelling. *Earth and Planetary Science Letters*, 357, 238-248.
- 822 3. Angiboust, S., Pettke, T., De Hoog, J. C., Caron, B., & Oncken, O. (2014).
823 Channelized fluid flow and eclogite-facies metasomatism along the subduction shear
824 zone. *Journal of petrology*, 55(5), 883-916.
- 825 4. Angiboust, S., Cambeses, A., Hyppolito, T., Glodny, J., Monié, P., Calderón, M., &
826 Juliani, C. (2018). A 100-my-long window onto mass-flow processes in the
827 Patagonian Mesozoic subduction zone (Diego de Almagro Island, Chile). *Bulletin*,
828 130(9-10), 1439-1456.
- 829 5. Angiboust, S., & Glodny, J. (2020). Exhumation of eclogitic ophiolitic nappes in the
830 W. Alps: New age data and implications for crustal wedge dynamics. *Lithos*, 356,
831 105374.
- 832 6. Barnes, C. J., Zack, T., Bukała, M., Rösel, D., Mark, C., & Schneider, D. A. (2024).
833 Dating metamorphic processes and identifying $87\text{Sr}/86\text{Sr}$ inheritance using volume-
834 coupled Rb/Sr geochronology and geochemistry of in situ white mica: A
835 demonstration with HP/LT rocks from Syros, Greece. *Chemical Geology*, 122149.
- 836 7. Bastias, J., Spikings, R., Riley, T., Chew, D., Grunow, A., Ulianov, A., ... & Burton-
837 Johnson, A. (2023). Cretaceous magmatism in the Antarctic Peninsula and its tectonic
838 implications. *Journal of the Geological Society*, 180(1), jgs2022-067.
- 839 8. Behr, W. M., Kotowski, A. J., & Ashley, K. T. (2018). Dehydration-induced
840 rheological heterogeneity and the deep tremor source in warm subduction zones.
841 *Geology*, 46(5), 475-478.
- 842 9. Behr, W. M., & Bürgmann, R. (2021). What's down there? The structures, materials
843 and environment of deep-seated slow slip and tremor. *Philosophical Transactions of
844 the Royal Society A*, 379(2193), 20200218.
- 845 10. v. Blanckenburg, F., Villa, I. M., Baur, H., Morteani, G., & Steiger, R. H. (1989).
846 Time calibration of a PT-path from the Western Tauern Window, Eastern Alps: the
847 problem of closure temperatures. *Contributions to mineralogy and Petrology*, 101(1),
848 1-11.
- 849 11. Breeding, C. M., Ague, J. J., & Bröcker, M. (2004). Fluid-metasedimentary rock
850 interactions in subduction-zone mélange: implications for the chemical composition
851 of arc magmas. *Geology*, 32(12), 1041-1044.
- 852 12. Bröcker, M., & Enders, M. (2001). Unusual bulk-rock compositions in eclogite-facies
853 rocks from Syros and Tinos (Cyclades, Greece): implications for U-Pb zircon
854 geochronology. *Chemical Geology*, 175(3-4), 581-603.
- 855 13. Bröcker, M., Baldwin, S., & Arkudas, R. (2013). The geological significance of
856 $40\text{Ar}/39\text{Ar}$ and Rb-Sr white mica ages from S yros and S ifnos, G reece: a record of
857 continuous (re) crystallization during exhumation?. *Journal of Metamorphic Geology*,
858 31(6), 629-646.



859 14. Burg, J. P., & Bouilhol, P. (2019). Timeline of the South Tibet–Himalayan belt: The
860 geochronological record of subduction, collision, and underthrusting from zircon and
861 monazite U–Pb ages. *Canadian Journal of Earth Sciences*, 56(12), 1318–1332.

862 15. Chew, D. M., & Spikings, R. A. (2015). Geochronology and thermochronology using
863 apatite: time and temperature, lower crust to surface. *Elements*, 11(3), 189–194.

864 16. Cisneros, M., Barnes, J. D., Behr, W. M., Kotowski, A. J., Stockli, D. F., & Soukis,
865 K. (2020). Insights from elastic thermobarometry into exhumation of high-pressure
866 metamorphic rocks from Syros, Greece. *Solid Earth Discussions*, 2020, 1–27.

867 17. Cooperdock, E. H., Raia, N. H., Barnes, J. D., Stockli, D. F., & Schwarzenbach, E. M.
868 (2018). Tectonic origin of serpentinites on Syros, Greece: Geochemical signatures of
869 abyssal origin preserved in a HP/LT subduction complex. *Lithos*, 296, 352–364.

870 18. Dalton, H., Giuliani, A., Phillips, D., Hergt, J., Maas, R., Matchan, E., ... & O'Brien,
871 H. (2020). A comparison of geochronological methods commonly applied to
872 kimberlites and related rocks: Three case studies from Finland. *Chemical Geology*,
873 558, 119899.

874 19. Ducharme, T. A., Schneider, D. A., Grasemann, B., Bukała, M., Camacho, A.,
875 Larson, K. P., & Soukis, K. (2024). Syn-exhumation metasomatic glaucophane-
876 phengite-quartz veins formed at moderate pressures: exploring the control of fO₂ and
877 bulk composition on nominally HP metamorphic assemblages. *Contributions to
878 Mineralogy and Petrology*, 179(3), 1–25.

879 20. Engi, M., Lanari, P., & Kohn, M. J. (2017). Significant ages—An introduction to
880 petrochronology. *Reviews in Mineralogy and Geochemistry*, 83(1), 1–12.

881 21. Fitzpayne, A., Giuliani, A., Hergt, J., Woodhead, J. D., & Maas, R. (2020). Isotopic
882 analyses of clinopyroxenes demonstrate the effects of kimberlite melt metasomatism
883 upon the lithospheric mantle. *Lithos*, 370, 105595.

884 22. Fitzpayne, A., Giuliani, A., Howarth, G. H., Peters, B. J., Fehr, M. A., & Maas, R.
885 (2023). Major-, trace-element and Sr–Nd–Hf isotope geochemistry of diamondiferous
886 dykes from Tonguma and Koidu, Sierra Leone: highly micaceous kimberlites formed
887 by assimilation of metasomatised lithospheric mantle rocks. *Chemical Geology*, 630,
888 121475.

889 23. Gautier, P., & Brun, J. P. (1994). Ductile crust exhumation and extensional
890 detachments in the central Aegean (Cyclades and Evvia Islands). *Geodinamica Acta*,
891 7(2), 57–85.

892 24. Giuliani, A., Oesch, S., Guillong, M., & Howarth, G. H. (2024). Mica RbSr dating by
893 laser ablation ICP-MS/MS using an isochronous calibration material and application
894 to West African kimberlites. *Chemical Geology*, 121982.

895 25. Glodny, J., Grauert, B., Fiala, J., Vejnar, Z., & Krohe, A. (1998). Metapegmatites in
896 the western Bohemian massif: ages of crystallisation and metamorphic overprint, as
897 constrained by U–Pb zircon, monazite, garnet, columbite and Rb–Sr muscovite data.
898 *Geologische Rundschau*, 87, 124–134.

899 26. Glodny, J., Pease, V., Montero, P., Austrheim, H., & Rusin, A. I. (2004). Protolith
900 ages of eclogites, Marun–Keu Complex, Polar Urals, Russia: implications for the pre-
901 and early Uralian evolution of the northeastern European continental margin.
902 *Geological Society, London, Memoirs*, 30(1), 87–105.

903 27. Glodny, J., Kühn, A., & Austrheim, H. (2008). Geochronology of fluid-induced
904 eclogite and amphibolite facies metamorphic reactions in a subduction–collision
905 system, Bergen Arcs, Norway. *Contributions to Mineralogy and Petrology*, 156, 27–
906 48.



907 28. Glodny, J., & Ring, U. (2022). The Cycladic Blueschist Unit of the Hellenic
908 subduction orogen: Protracted high-pressure metamorphism, decompression and
909 reimplication of a diachronous nappe stack. *Earth-Science Reviews*, 224, 103883.

910 29. Gou, L. L., Long, X. P., Yan, H. Y., Shu, T. C., Wang, J. Y., Xu, X. F., ... & Tian, Z.
911 B. (2022). Metamorphic P-T Evolution and In Situ Biotite Rb-Sr Geochronology of
912 Garnet-Staurolite Schist From the Ramba Gneiss Dome in the Northern Himalaya.
913 *Frontiers in Earth Science*, 10, 887154.

914 30. Gyomlai, T., Agard, P., Jolivet, L., Larvet, T., Bonnet, G., Omrani, J., ... & Noël, J.
915 (2022). Cimmerian metamorphism and post Mid-Cimmerian exhumation in Central
916 Iran: Insights from in-situ Rb/Sr and U/Pb dating. *Journal of Asian Earth Sciences*,
917 233, 105242.

918 31. Gyomlai, T., Agard, P., Marschall, H. R., & Jolivet, L. (2023a). Hygrochronometry of
919 punctuated metasomatic events during exhumation of the Cycladic blueschist unit
920 (Syros, Greece). *Terra Nova*, 35(2), 101-112.

921 32. Gyomlai, T., Agard, P., Herviou, C., Jolivet, L., Monié, P., Mendes, K., & Iemmolò,
922 A. (2023b). In situ Rb-Sr and 40Ar-39Ar dating of distinct mica generations in the
923 exhumed subduction complex of the Western Alps. *Contributions to Mineralogy and
924 Petrology*, 178(9), 58.

925 33. Halama, R., John, T., Herms, P., Hauff, F., & Schenk, V. (2011). A stable (Li, O) and
926 radiogenic (Sr, Nd) isotope perspective on metasomatic processes in a subducting
927 slab. *Chemical Geology*, 281(3-4), 151-166.

928 34. Halama, R., Konrad-Schmolke, M., & De Hoog, J. C. (2020). Boron isotope record of
929 peak metamorphic ultrahigh-pressure and retrograde fluid–rock interaction in white
930 mica (Lago di Cignana, Western Alps). *Contributions to Mineralogy and Petrology*,
931 175(3), 20.

932 35. Holtmann, R., Muñoz-Montecinos, J., Angiboust, S., Cambeses, A., Bonnet, G.,
933 Brown, A., ... & Agard, P. (2022). Cretaceous thermal evolution of the closing Neo-
934 Tethyan realm revealed by multi-method petrochronology. *Lithos*, 422, 106731.

935 36. Huang, C., Wang, H., Shi, W., Sun, J., Hu, F., Xu, L., ... & Yang, J. (2023). In situ
936 Rb-Sr dating of mica by LA-ICP-MS/MS. *Science China Earth Sciences*, 66(11),
937 2603-2621.

938 37. Hyppolito, T., Angiboust, S., Juliani, C., Glodny, J., Garcia-Casco, A., Calderón, M.,
939 & Chopin, C. (2016). Eclogite-, amphibolite-and blueschist-facies rocks from Diego
940 de Almagro Island (Patagonia): Episodic accretion and thermal evolution of the
941 Chilean subduction interface during the Cretaceous. *Lithos*, 264, 422-440.

942 38. John, T., Gussone, N., Podladchikov, Y. Y., Bebout, G. E., Dohmen, R., Halama, R.,
943 ... & Seitz, H. M. (2012). Volcanic arcs fed by rapid pulsed fluid flow through
944 subducting slabs. *Nature Geoscience*, 5(7), 489-492.

945 39. Jolivet, L., Lecomte, E., Huet, B., Denèle, Y., Lacombe, O., Labrousse, L., ... & Mehl,
946 C. (2010). The north cycladic detachment system. *Earth and Planetary Science
947 Letters*, 289(1-2), 87-104.

948 40. Keay, S., 1998. The Geological Evolution of the Cyclades, Greece: Constraints from
949 SHRIMP U-Pb Geochronology. Unpublished PhD Thesis . Australian National
950 University , Canberra .

951 41. Keiter, M., Ballhaus, C., & Tomaschek, F. (2011). A new geological map of the
952 Island of Syros (Aegean Sea, Greece): Implications for lithostratigraphy and structural
953 history of the Cycladic Blueschist Unit (Vol. 481). *Geological Society of America*.

954 42. Kirchner, K. L., Behr, W. M., Loewy, S., & Stockli, D. F. (2016). Early Miocene
955 subduction in the western Mediterranean: Constraints from Rb-Sr multimineral
956 isochron geochronology. *Geochemistry, Geophysics, Geosystems*, 17(5), 1842-1860.



957 43. Kirkland, C. L., Olierook, H. K., Danišík, M., Liebmann, J., Hollis, J., Ribeiro, B. V.,
958 & Rankenburg, K. (2023). Dating mylonitic overprinting of ancient rocks.
959 Communications Earth & Environment, 4(1), 47.

960 44. Kleine, B. I., Skelton, A. D., Huet, B., & Pitcairn, I. K. (2014). Preservation of
961 blueschist-facies minerals along a shear zone by coupled metasomatism and fast-
962 flowing CO₂-bearing fluids. Journal of Petrology, 55(10), 1905-1939.

963 45. Kotowski, A. J., Cisneros, M., Behr, W. M., Stockli, D. F., Soukis, K., Barnes, J. D.,
964 & Ortega-Arroyo, D. (2022). Subduction, underplating, and return flow recorded in
965 the Cycladic Blueschist Unit exposed on Syros, Greece. Tectonics, 41(6),
966 e2020TC006528.

967 46. Kutzschbach, M., & Glodny, J. (2024). LA-ICP-MS/MS-based Rb–Sr isotope
968 mapping for geochronology. Journal of Analytical Atomic Spectrometry, 39(2), 455-
969 477.

970 47. Lagos, M., Scherer, E. E., Tomaschek, F., Münker, C., Keiter, M., Berndt, J., &
971 Ballhaus, C. (2007). High precision Lu–Hf geochronology of Eocene eclogite-facies
972 rocks from Syros, Cyclades, Greece. Chemical Geology, 243(1-2), 16-35.

973 48. Laurent, V., Lanari, P., Naïr, I., Augier, R., Lahfid, A., & Jolivet, L. (2018).
974 Exhumation of eclogite and blueschist (Cyclades, Greece): Pressure–temperature
975 evolution determined by thermobarometry and garnet equilibrium modelling. Journal
976 of metamorphic geology, 36(6), 769-798.

977 49. Li, K., Li, G. Y., Du, Y. F., Han, W., Zhang, J., Chen, L. H., ... & Li, L. (2021).
978 Intraslab remobilization of nitrogen during early subduction facilitates deep nitrogen
979 recycling: Insights from the blueschists in the Heilongjiang Complex in NE China.
980 Chemical Geology, 583, 120474.

981 50. Muñoz-Montecinos, J., Angiboust, S., Cambeses, A., & García-Casco, A. (2020).
982 Multiple veining in a paleo–accretionary wedge: The metamorphic rock record of
983 prograde dehydration and transient high pore-fluid pressures along the subduction
984 interface (Western Series, central Chile). Geosphere, 16(3), 765-786.

985 51. Muñoz-Montecinos, J., Angiboust, S., & Garcia-Casco, A. (2021). Blueschist-facies
986 paleo-earthquakes in a serpentinite channel (Zagros suture, Iran) enlighten
987 seismogenesis in Marianas-type subduction margins. Earth and Planetary Science
988 Letters, 573, 117135.

989 52. Muñoz-Montecinos, J., & Behr, W. M. (2023). Transient Permeability of a Deep-
990 Seated Subduction Interface Shear Zone. Geophysical Research Letters, 50(20),
991 e2023GL104244.

992 53. Olierook, H. K., Rankenburg, K., Ulrich, S., Kirkland, C. L., Evans, N., Brown, S., ...
993 & Darragh, M. (2020). Resolving multiple geological events using in situ Rb–Sr
994 geochronology: implications for metallogenesis at Tropicana, Western Australia.
995 Geochronology Discussions, 2020, 1-31.

996 54. Paton, C., Woodhead, J. D., Hergt, J. M., Phillips, D., & Shee, S. (2007). Strontium
997 isotope analysis of kimberlitic groundmass perovskite via LA-MC-ICP-MS.
998 Geostandards and Geoanalytical Research, 31(4), 321-330.

999 55. Paton, C., Hellstrom, J., Paul, B., Woodhead, J., & Hergt, J. (2011). Iolite: Freeware
1000 for the visualisation and processing of mass spectrometric data. Journal of Analytical
1001 Atomic Spectrometry, 26(12), 2508-2518.

1002 56. Phillips, D., Zhong, D., Matchan, E. L., Maas, R., Farr, H., O'Brien, H., & Giuliani,
1003 A. (2017, September). A comparison of geochronology methods applied to
1004 kimberlites and related rocks from the Karelian Craton, Finland. In International
1005 Kimberlite Conference: Extended Abstracts (Vol. 11).



1006 57. Pimenta Silva, M., Marxer, F., Keller, T., Giuliani, A., Ulmer, P., & Müntener, O.
1007 (2023). Alkaline magmas in shallow arc plutonic roots: a field and experimental
1008 investigation of hydrous cumulate melting in the southern Adamello batholith.
1009 Contributions to Mineralogy and Petrology, 178(9), 64.

1010 58. Plank, T. (2014). The chemical composition of subducting sediments. Elsevier.

1011 59. Pirlitz, B., Cosca, M. A., & Schumacher, J. C. (2005). Prograde mica 40Ar/39Ar
1012 growth ages recorded in high pressure rocks (Syros, Cyclades, Greece). Chemical
1013 Geology, 214(1-2), 79-98.

1014 60. Redaa, A., Farkaš, J., Gilbert, S., Collins, A. S., Wade, B., Löhr, S., ... & Garbe-
1015 Schönberg, D. (2021). Assessment of elemental fractionation and matrix effects
1016 during in situ Rb-Sr dating of phlogopite by LA-ICP-MS/MS: implications for the
1017 accuracy and precision of mineral ages. Journal of Analytical Atomic Spectrometry,
1018 36(2), 322-344.

1019 61. Ribeiro, B. V., Kirkland, C. L., Finch, M. A., Faleiros, F. M., Reddy, S. M., Rickard,
1020 W. D., & Michael, I. H. (2023). Microstructures, geochemistry, and geochronology of
1021 mica fish: Review and advances. Journal of Structural Geology, 104947.

1022 62. Rubatto, D., Williams, M., Markmann, T. A., Hermann, J., & Lanari, P. (2023).
1023 Tracing fluid infiltration into oceanic crust up to ultra-high-pressure conditions.
1024 Contributions to Mineralogy and Petrology, 178(11), 79.

1025 63. Salters, V. J., & Stracke, A. (2004). Composition of the depleted mantle.
1026 Geochemistry, Geophysics, Geosystems, 5(5).

1027 64. Sarkar, S., Giuliani, A., Dalton, H., Phillips, D., Ghosh, S., Misev, S., & Maas, R.
1028 (2023). Derivation of Lamproites and Kimberlites from a Common Evolving Source
1029 in the Convective Mantle: the Case for Southern African 'Transitional Kimberlites'.
1030 Journal of Petrology, 64(7), egad043.

1031 65. Schmidt, M. W., Vielzeuf, D., & Auzanneau, E. (2004). Melting and dissolution of
1032 subducting crust at high pressures: the key role of white mica. Earth and Planetary
1033 Science Letters, 228(1-2), 65-84.

1034 66. Seman, S., Stockli, D. F., & Soukis, K. (2017). The provenance and internal structure
1035 of the Cycladic Blueschist Unit revealed by detrital zircon geochronology, Western
1036 Cyclades, Greece. Tectonics, 36(7), 1407-1429.

1037 67. Smit, M. A., & von Strandmann, P. A. P. (2020). Deep fluid release in warm
1038 subduction zones from a breached slab seal. Earth and Planetary Science Letters, 534,
1039 116046.

1040 68. Soukis, K., & Stockli, D. F. (2013). Structural and thermochronometric evidence for
1041 multi-stage exhumation of southern Syros, Cycladic islands, Greece. Tectonophysics,
1042 595, 148-164.

1043 69. Tewksbury-Christle, C. M., Behr, W. M., & Helper, M. A. (2021). Tracking deep
1044 sediment underplating in a fossil subduction margin: Implications for interface
1045 rheology and mass and volatile recycling. Geochemistry, Geophysics, Geosystems,
1046 22(3), e2020GC009463.

1047 70. Tillberg, M., Drake, H., Zack, T., Kooijman, E., Whitehouse, M. J., & Åström, M. E.
1048 (2020). In situ Rb-Sr dating of slickenfibres in deep crystalline basement faults.
1049 Scientific reports, 10(1), 562.

1050 71. Tillberg, M., Drake, H., Zack, T., Hogmalm, J., Kooijman, E., & Åström, M. (2021).
1051 Reconstructing craton-scale tectonic events via in situ Rb-Sr geochronology of poly-
1052 phased vein mineralization. Terra Nova, 33(5), 502-510.

1053 72. Tomaschek, F., Kennedy, A. K., Villa, I. M., Lagos, M., & Ballhaus, C. (2003).
1054 Zircons from Syros, Cyclades, Greece—recrystallization and mobilization of zircon
1055 during high-pressure metamorphism. Journal of Petrology, 44(11), 1977-2002.



1056 73. Trotet, F., Jolivet, L., & Vidal, O. (2001). Tectono-metamorphic evolution of Syros
1057 and Sifnos islands (Cyclades, Greece). *Tectonophysics*, 338(2), 179-206.

1058 74. Rajič, K., Raimbourg, H., Gion, A. M., Lerouge, C., & Erdmann, S. (2024). Tracing
1059 the Scale of Fluid Flow in Subduction Zone Forearcs: Implications from Fluid-Mobile
1060 elements. *Chemical Geology*, 122141.

1061 75. Redaa, A., Farkaš, J., Hassan, A., Collins, A. S., Gilbert, S., & Löhr, S. C. (2022).
1062 Constraints from in-situ Rb-Sr dating on the timing of tectono-thermal events in the
1063 Umm Farwah shear zone and associated Cu-Au mineralisation in the Southern
1064 Arabian Shield, Saudi Arabia. *Journal of Asian Earth Sciences*, 224, 105037.

1065 76. Taylor, A. S., & Lasaga, A. C. (1999). The role of basalt weathering in the Sr isotope
1066 budget of the oceans. *Chemical Geology*, 161(1-3), 199-214.

1067 77. Timmermann, H., Štědrá, V., Gerdes, A., Noble, S. R., Parrish, R. R., & Dörr, W.
1068 (2004). The problem of dating high-pressure metamorphism: a U-Pb isotope and
1069 geochemical study on eclogites and related rocks of the Mariánské Lázně Complex,
1070 Czech Republic. *Journal of Petrology*, 45(7), 1311-1338.

1071 78. Tumiati, S., Recchia, S., Remusat, L., Tiraboschi, C., Sverjensky, D. A., Manning, C.
1072 E., ... & Poli, S. (2022). Subducted organic matter buffered by marine carbonate rules
1073 the carbon isotopic signature of arc emissions. *Nature Communications*, 13(1), 2909.

1074 79. Zack, T., & Roesel, D. (2021, December). Towards robust in-situ Rb-Sr spot ages. In
1075 AGU Fall Meeting Abstracts (Vol. 2021, pp. V22A-04).

1076 80. Uunk, B., Brouwer, F., ter Voorde, M., & Wijbrans, J. (2018). Understanding
1077 phengite argon closure using single grain fusion age distributions in the Cycladic
1078 Blueschist Unit on Syros, Greece. *Earth and Planetary Science Letters*, 484, 192-203.

1079 81. Vermeesch, P. (2018). IsoplotR: A free and open toolbox for geochronology.
1080 *Geoscience Frontiers*, 9(5), 1479-1493.

1081 82. Villa, I. M. (1998). Isotopic closure. *Terra nova*, 10(1), 42-47.

1082 83. Villa, I. M. (2016). Diffusion in mineral geochronometers: Present and absent.
1083 *Chemical Geology*, 420, 1-10.

1084 84. Voigt, M., Pearce, C. R., Baldermann, A., & Oelkers, E. H. (2018). Stable and
1085 radiogenic strontium isotope fractionation during hydrothermal seawater-basalt
1086 interaction. *Geochimica et Cosmochimica Acta*, 240, 131-151.

1087 85. Volante, S., Blereau, E., Guitreau, M., Tedeschi, M., van Schijndel, V., & Cutts, K.
1088 (2024). Current applications using key mineral phases in igneous and metamorphic
1089 geology: perspectives for the future. *Geological Society, London, Special
1090 Publications*, 537(1), 57-121.

1091 86. Wang, C., Alard, O., Lai, Y. J., Foley, S. F., Liu, Y., Munnikhuis, J., & Wang, Y.
1092 (2022). Advances in in-situ Rb-Sr dating using LA-ICP-MS/MS: applications to
1093 igneous rocks of all ages and to the identification of unrecognized metamorphic
1094 events. *Chemical Geology*, 610, 121073.

1095 87. Wawrzenitz, N., Romer, R. L., Oberhänsli, R., & Dong, S. (2006). Dating of
1096 subduction and differential exhumation of UHP rocks from the Central Dabie
1097 Complex (E-China): constraints from microfabrics, Rb-Sr and U-Pb isotope systems.
1098 *Lithos*, 89(1-2), 174-201.

1099 88. Whitney, D. L., & Evans, B. W. (2010). Abbreviations for names of rock-forming
1100 minerals. *American mineralogist*, 95(1), 185-187.

1101 89. Wirth, E. A., Sahakian, V. J., Wallace, L. M., & Melnick, D. (2022). The occurrence
1102 and hazards of great subduction zone earthquakes. *Nature Reviews Earth &
1103 Environment*, 3(2), 125-140.

1104 90. Zack, T., & John, T. (2007). An evaluation of reactive fluid flow and trace element
1105 mobility in subducting slabs. *Chemical Geology*, 239(3-4), 199-216.



1106 91. Zametzer, A., Kirkland, C. L., Barham, M., Hartnady, M. I., Bath, A. B., &
1107 Rankenburg, K. (2022). Episodic alteration within a gold-bearing Archean shear zone
1108 revealed by in situ biotite Rb–Sr dating. *Precambrian Research*, 382, 106872.
1109 92. Zhao, H., Zhao, X. M., Le Roux, P. J., Zhang, W., Wang, H., Xie, L. W., ... & Yang,
1110 Y. H. (2020). Natural clinopyroxene reference materials for in situ Sr isotopic
1111 analysis via LA-MC-ICP-MS. *Frontiers in Chemistry*, 8, 594316.
1112